POLITECNICO DI TORINO

Master of Science in Biomedical Engineering

-Biomechanics-

Master's Thesis

AESO-based composites filled with biochar obtained by LCD 3D printing

Supervisor

Prof.ssa Giovanna Colucci

Co-supervisor

Prof. Massimo Messori

Candidate

Federica Di Stefano

S292205

Academic Year 2023/2024

LIST OF ACRONYMS

3DP: 3D printing

AESO: Acrylate epoxidized soybean oil

AM: Additive manufacturing

BAPO: Phenylbis (2,4,6-trimethylbenzoyl) phosphine oxide

CLIP: Continuous liquid interface

CNC: Crystalline nanocellulose

DLP: Direct light processing

DMTA: Dynamic mechanical thermal analysis

DSC: Differential scanning calorimetry

DPP: Daylight polymer printing

FEG: Field emission gun

FESEM: Field-emission scanning electron microscope

FFF: Fused Filament Fabrication

IBOMA: Iso bornyl methacrylate

LCD: Liquid crystal display

phr: parts per hundred resin

PI: Photoinitiator

PPI: Pixels Per Inch

RD: Reactive diluent

RT: Room temperature

SLA: Stereolithography

STL: Standard tessellation language

TGA: Thermogravimetric analysis

VOs: Vegetable oils

LIST OF FIGURES

LIST OF TABLES

Table of Contents

ABSTRACT

Additive manufacturing (AM) techniques have gained attention in the scientific community for their ability to rapidly produce components with intricate shapes based on computer-generated designs. These techniques offer numerous benefits for composite manufacturing, including high accuracy, cost-effectiveness, and the ability to create custom geometries reducing material waste.

Polymers and polymeric composites are extensively employed in contemporary industries and hold significant interest in AM, especially for applications in the medical, aerospace, and automotive sectors. Nevertheless, most polymers are currently derived from non-renewable fossil feedstocks and are highly resistant to biodegradation, leading to increasing plastic pollution. This poses a serious global environmental threat, impacting land, water, and air quality.

As a result, academic research and the manufacturing industry are facing a growing need to replace fossil-based polymers with bio-based alternatives.

The aim of the present thesis work was the preparation and characterisation of bio-based photocured composites using photocurable thermosetting polymers by 3D printing (3DP).

Acrylate epoxidized soybean oil (AESO) at 50% w/w was selected as the monomeric starting material, and 50% w/w of isobornyl methacrylate (IBOMA) was used as a reactive diluent, to improve the 3D printability of the AESO by reducing its high viscosity. A 2phr amount of phenylbis(2,4,6-trimethylbenzoyl) phosphine oxide (BAPO) was incorporated as a radical photoinitiator (PI) to promote the photopolymerisation process, which was carried out by using a vat photopolymerisation technique in a liquid crystal display (LCD) 3D printer.

Biochar, a carbonaceous biofiller derived from biomass pyrolysis, was added at concentrations of 0.5, 1, and 2 phr to enhance the properties of the starting resin. Biomass is abundant, renewable, and sustainable, making biochar a valuable solution for various applications, offering great potential to replace fossil fuel resources.

Rheological measurements were first performed to evaluate the viscosity and printability of the prepared photocurable formulations. After determining the optimal printing

parameters for all formulations, with and without biochar, various geometries were successfully 3D printed, progressively leading to the realization of more complex objects with a varying number of layers and good dimensional accuracy.

Finally, the polymeric compounds underwent characterisation tests to investigate the resulting properties. Tensile tests were performed to analyse mechanical properties, in terms of elastic modulus, tensile strength and deformation. Thermogravimetric analysis (TGA) and differential scanning calorimetry (DSC) were carried out to examine the thermal stability and thermal behaviour. Dynamic mechanical analysis (DMTA) was performed to investigate the viscoelastic properties of the final composites. Morphological characterisations were also carried out to evaluate the dispersion of the biochar within the photocured polymeric composites, by using field emission scanning electron microscopy (FESEM), which provided high-quality images of the 3D printed specimens.

The results of this research work reveal biochar-filled soybean oil resins as good candidates for the 3D printing of polymeric materials, representing effective sustainable alternatives to conventional ones and fostering a more eco-friendly and environmentally respectful future.

INTRODUCTION

Plastics are defined as a subset of polymers that contain long-chain organic molecules with desired characteristics, having various advantages in comparison to metals, wood and ceramics. [1]

For instance, plastics are lightweight, affordable, chemically inert, flexible, easily shaped and highly functional. [2]

Due to their versatility, they are key materials in packaging, building, transportation, medical devices, automotive, etc. In 2016, global plastics production reached 335 million tons, highlighting their widespread use and popularity. [3]

According to open data by Plastics Europe [4], production increased to approximately 370 million tons by 2019 and, with continued annual growth, is projected to exceed 800 million tons worldwide by 2050. [1] After a slowdown in 2020 due to the COVID-19 pandemic, output rose again, reaching 390.7 million tons in 2021 (Figure 1).

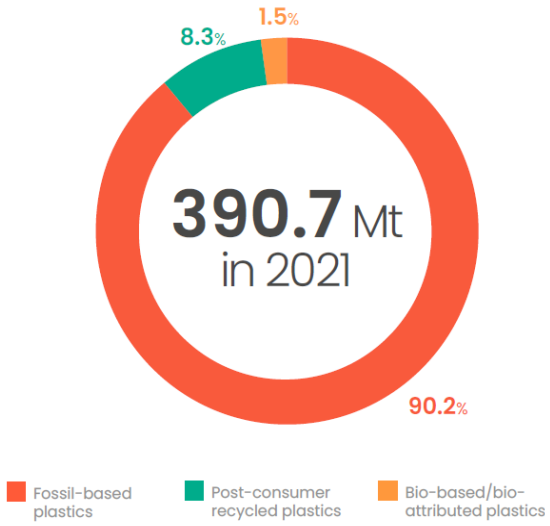

Figure 1. World plastic production in 2021. [4]

Despite their large-scale production and widespread applications, plastics generally have short lifespans. Once they reach the end of their useful life, these previously valuable materials lose their economic worth.

Their disposal methods are often unclear, with less than 9% being recycled. Approximately 80% of plastic products end up as waste, entering environments such as land, oceans, and

rivers. This leads to substantial economic losses, estimated between 80 and 120 billion USD each year. [1]

Moreover, the strength and resilience of polymers enhance their performance but also raise serious environmental concerns. Plastics degrade very slowly, often persisting in their original form for decades or even centuries. [1] Their extended stability is one of the key factors contributing to environmental harm.

According to the World Meteorological Organization, the year 2023 set unprecedented climate records, becoming the warmest year on record, with global temperatures rising to 1.45°C. [5]

In line with the Sustainable Development Goals, adopted by The United Nations Member States in 2015 as part of the 2030 Agenda for Sustainable Development [6], and particularly with Goal 13, which demands Climate Action, but also with Goal 12, which demands responsible consumption and production, over the past decade significant efforts have been directed toward developing sustainable polymers, with many scientists embracing the challenge of creating new materials from renewable, bio-based resources. Both Goal 12 and Goal 13 symbols are shown in Figure 2.

Figure 2. Sustainable Development Goals of the 2030 Agenda. [6]

The present work is positioned within the described field, to advance research on 3DP novel sustainable bio-based thermosets using a vat photopolymerisation technique. In such technology, replacing petroleum-based materials with those derived from renewable resources offers both ecological and economic benefits, including lower toxicity, higher biodegradability, improved recovery and recycling options, and a reduction in greenhouse gas emissions. [7]

This study explores the use of soybean oil-derived resins, modified through epoxidation and acrylation, to be compatible with UV-photopolymerisation in 3D printing. To improve their mechanical and thermal properties, biochar, a bio-filler coming from biomass pyrolysis, is added, thereby utilizing renewable resources.

AIM OF THE WORK

The aim of this thesis is to study and develop new formulations of thermosetting resins derived from plant-based materials, specifically designed for additive manufacturing (AM) techniques, with a particular focus on LCD printing, as method of vat photopolymerisation. Compared to other conventional techniques, LCD printing stands out for its cost-effectiveness and its ability to produce high-quality results in terms of resolution of the final objects and printing speed.

The decision to use bio-based materials is driven by the increasing demand within the manufacturing industry and scientific research to replace thermosetting plastics derived from fossil fuels with renewable resources, thereby promoting environmental sustainability and minimizing the ecological footprint of industrial production.

The starting monomeric material chosen for this study is acrylate epoxidized soybean oil (AESO), diluted with isobornyl methacrylate (IBOMA), and combined with a photoinitiator, phenylbis (2,4,6-trimethylbenzoyl) phosphine oxide (BAPO), to initiate the photopolymerisation process necessary for this printing technology. Furthermore, a composite mixture is prepared by adding biochar in varying concentrations to enhance the mechanical properties and thermal stability of the resin.

After selecting the formulation components, the research focuses on identifying the optimal printing parameters that guarantee high performance in terms of stability, surface quality, and layer adhesion. A comprehensive series of tests were carried out to analyse the morphological, thermal, mechanical, and rheological properties of the composites produced with this photocurable resin.

The goal was to support the advancement of production technologies that aligns with the principles of circular economy and environmental sustainability. By encouraging the use of renewable resources and reducing dependence on fossil-derived materials, this work aspires to foster innovation in additive manufacturing, promoting a more sustainable industrial future that prioritizes both technological progress and the preservation of natural ecosystems for future generations.

1. POLYMERS

Polymers are large molecules formed by the repeated linking of numerous smaller molecules called monomers, which join to create polymer chains, and the processes through which they bond are known as polymerisation reactions. [8]

1.1. NATURAL AND SYNTHESIZED POLYMERS

Polymers can be classified based on various criteria. One common classification, according to sources, distinguishes between natural and synthetic polymers:

- *Natural polymers* are found in nature. Examples include rubber, protein or cellulose. Since plants and trees are primarily composed of cellulose, it is the most abundant polymer on Earth. [9]
- *Synthesized polymers* are produced through chemical synthesis in laboratories or industrial settings and have longer chains compared to natural polymers. They are mainly derived from petroleum, which is both plentiful and affordable. Common examples of synthetic polymers include polystyrene, polypropylene, polyethylene, which find extensive use in packaging, textiles, and consumer goods, but also Bakelite or Bisphenol A. These polymers can be engineered to exhibit specific properties, such as enhanced strength, elasticity, or chemical resistance, making them highly versatile. However, unlike natural polymers, synthetic polymers often lack biodegradability and can pose environmental challenges if not properly managed.

1.2. THERMOPLASTICS, ELASTOMERS AND THERMOSETTINGS

Based on thermal properties, polymers can be classified into thermoplastics, elastomers, and thermosettings.

1.2.1 Thermoplastics

Thermoplastics polymers can be shaped under heating. When heated above a certain temperature, they become highly viscous liquids that can be moulded into different forms; once cooled, they keep the shape of the mould. This heating and moulding process can generally be repeated multiple times; however, after several cycles, the polymer chains

may break down or react, leading to a decline in physical properties, which limits the recyclability of thermoplastics. A schematic representation of the structure of a thermoplastic polymer is reported in Figure 3. In this figure, the polymer is represented with long, linear chains of monomers linked by covalent bonds. This structure, typical of thermoplastics, imparts significant flexibility and mobility, essential for reshaping during heating. In fact, the linear configuration enables the polymer chains to move freely when heated, facilitating the transformation of the material into a viscous liquid that can be easily moulded.

Figure 3. Schematic structure of a thermoplastic. [10]

The degree of crystallinity of polymers can affect their properties. Both semicrystalline and amorphous thermoplastics behave like viscous liquids when the temperature is above their glass transition temperature (Tg), while below Tg, they become hard and rigid, like glass. Some of the most common thermoplastics are polyethylene, both low-density polyethylene (LDPE) and high-density polyethylene (HDPE), poly(vinyl chloride) (PVC), polypropylene (PP), and polystyrene (PS). [11]

1.2.2. Elastomers

Elastomers, commonly known as *rubbers*, are flexible materials that demonstrate high resistance to impact, even at low temperatures where most materials become more rigid. In many applications, such as tyres or hoses, these materials need to be slightly crosslinked after being shaped to provide dimensional stability; otherwise, they tend to deform over time. Elastomers are polymers used above their Tg, which ensures their flexibility. To name a few, some well-known examples include polybutadiene, used as an impact modifier in rigid plastics; SBR (a copolymer of styrene and butadiene), predominantly used in tyre production; EPDM (a copolymer of ethylene, propylene, and a diene monomer, typically norbornene. [11]

1.2.3. Thermosettings

Thermosettings, also called *Thermosets*, are amorphous polymers produced by the mixing and chemical reaction of fluid precursors within a mould. The term amorphous refers to the lack of long-range order in the arrangement of the polymer chains, which contrasts sharply with the ordered arrangement found in crystalline materials.

The initial liquid solution is usually composed of several ingredients. Firstly, a mixture of comonomers that can react among themselves, or undergo self-reaction of a single monomer, by an external action such as heating, UV-irradiation, etc. The rest of the reagents can be initiators, catalysts, fillers, or pigments. [11]

Figure 4 provides a schematic representation of a thermoset polymer structure. The grey dots illustrate the covalent bonds formed between polymeric chains during the curing process. These bonds are crucial because they create a crosslinked network that defines the properties of thermosetting materials. [11]

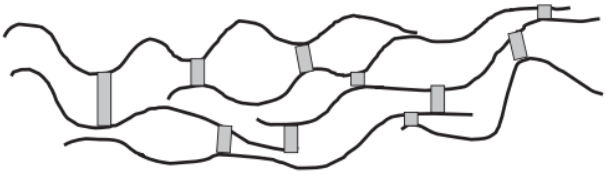

Figure 4. Thermosets after cross-linking. [10]

The curing chemical reaction in a thermoset is irreversible. Turning the resulting material into a liquid state would require the breaking of the generated covalent chemical bonds, a process that leads to the degradation of the material instead of the recuperation of the initial comonomers. So, once cured, the final product can't be reshaped, and this represents a drawback as it prevents recycling.

Common examples of thermosets include certain polyesters, phenol-formaldehyde resins, epoxy resins, and polyurethanes.

1.2.3.1 Thermosetting polymers formulation

The monomers, comonomers (hardeners), catalysts, and initiators are the key components that determine the characteristics of a thermosetting polymer. Depending on the desired properties of the final material, additional components may be included in the

formulation. Fillers, for example, are often added to enhance mechanical properties and/or to reduce production costs [12].

Owing to the excellent dimensional stability and outstanding mechanical and thermal properties from their covalently cross-linked network structures, thermosets have played an important and irreplaceable role in adhesives, composites, in electronic packaging materials, coatings [13], but also in various applications like transportation and construction. If combined with carbon and glass fibres to make composites, it is also possible to use them in advanced applications, such as in aerospace and military industries. [10]

Thermosets are polymers mainly derived from fossil resources with an estimated annual production of ~65 million tons. In recent years, scientific research has increasingly focused on the renewability of resources, leading to the development of various thermosetting materials derived from bio-based sources like plant oils, rosin, lignin, itaconic acid, isosorbide, cardanol, vanillin, and others. [13]

1.3. BIO-BASED POLYMERS

On a global trend, plastic production from fossil-based resources and plastic waste incineration together account for about 400 million tonnes of CO_2 every year. [14]

Consequently, as also shown in Figure 5 by the European Bioplastics website, in terms of fossil oil depletion and environmental concerns, the focus has increasingly been on the partial or complete replacement of petroleum-derived products with bio-based materials. [15]

Figure 5. From European Bioplastics. [4]

Bio-based polymers are materials produced from biomass resources. Biomass refers to the renewable organic material originating from plants, animals, and micro-organisms. It is abundantly available in nature and can be conveniently obtained at a low cost.

In particular, the development of thermosets from biomass is now attracting attention as a step towards sustainability. [15]

However, the direct usage of most biomass resources is often impractical and inefficient due to their complex structures. To enhance their utilization, biomass must be converted into simpler or more functional molecules, known as platform chemicals. There are two primary pathways for converting renewable feedstocks into bio-based platform chemicals: fermentation and chemical treatment. Nevertheless, many bio-based platform compounds are directly sourced from nature, such as rosin acids, vegetable oils (VOs), terpenes and terpenoids. [15]

These platform chemicals have several benefits in addition to sustainability and renewability, such as low toxicity and economic viability. Consequently, in the last decades, a wide range of natural feedstocks and biomass-derived monomers, such as lignin, itaconic acid, furan compounds, and vegetable oils, have undergone significant development in bio-based resins. [15]

Nowadays, vegetable oils, such as olive oil, linseed oil and soybean oil, are the most studied bio-resources in scientific literature. Their application as starting materials for producing bio-based polymers is particularly noteworthy due to their abundance and the presence of triglycerides, which can be modified to introduce functional groups for further polymerisation. [16]

Among vegetable oils, soybean oil has a similar structure as petroleum-based monomers, making it an alternative to petroleum-based biopolymers. [17] However, pure soybean oil resin does not provide adequate mechanical properties for engineering applications. As a result, it is commonly blended with fillers or fibres to produce polymer composites that can be utilized in biomedical, mechanical, or electronic applications. [18]

In this thesis, acrylate epoxidized soybean oil is utilized as the bio-based monomeric source, with biochar incorporated to enhance its mechanical properties, allowing for the development of printable photocured composites suitable for additive manufacturing applications.

2. ADDITIVE MANUFACTURING

Polymers and their composites are among the most widely used materials in modern industries and hold a significant interest in additive manufacturing thanks to their broad potential for diverse applications, particularly in the medical, aerospace, and automotive sectors. [19]

One of the key advantages of AM is its relatively constant production cost, which remains largely unaffected by both production scale and the complexity of the product's shape. Additionally, the minimal waste generated by this process makes it more environmentally friendly, offering a more sustainable alternative to traditional manufacturing methods. As a result, AM technology has experienced significant growth in popularity over the past decade. [20]

Also known as 3D printing (3DP), AM is a process in which a three-dimensional object is built from a computer-aided design (CAD) model, usually by successively adding materials in a layer-by-layer fashion. Instead of using cutting tools in machining processes, AM uses a heat source (laser or electron beam), ultraviolet (UV) light, or binding agent to achieve the deposition of materials. After one layer is built, the AM stage moves by a layer thickness so that another layer can be deposited. This process continues until the final part is fabricated [21].

2.1. AM GENERAL STEPS

Additive manufacturing processes are generally categorized into 7 phases.

STEP 1: CAD MODEL

The initial step in the AM process involves producing a three-dimensional (3D) model. Typically, the most common method for creating a 3D digital solid model is using CAD software. Alternatively, reverse engineering tools like 3D scanners can be employed to recreate the model of an existing object if the original design is unavailable. The objective of this step is to create the geometry of the part that will undergo additive manufacturing. [21]

STEP 2: STL MODEL CONVERSION

Through the conversion in standard tessellation language (STL) format, the CAD model is represented by triangular facets defined by vertices and normal, capturing only the surface geometry of the 3D object. [21]

STEP 3: STL MODEL SLICING

As additive manufacturing (AM) is a layer-by-layer fabrication process, the STL model must be sliced into multiple cross-sections (layers). The printing process builds each layer on top of the previously printed one, continuing until the entire model is completed. [21]

STEP 4: TOOLPATH AND G-CODE GENERATION

After slicing the model into layers, the toolpath is generated and then converted into G-code, a format recognized by the additive manufacturing system. This G-code directs the printing system to build the part layer by layer. [21]

STEP 5: MACHINE SETUP AND BUILD

Before starting the printing process, the AM machine must be properly configured. Key parameters to consider include material type, power, layer thickness, travel speed and support structure. These settings must be carefully chosen to ensure successful printing. Once the process has started, most AM machines operate automatically and require minimal monitoring. [21]

STEP 6: REMOVAL OF PRINTED OBJECTS

In this step, the printed object is removed, and in most AM technologies, this is done simply by separating it from the build plate. [21]

STEP 7: POST-PROCESSING

Post-processing procedures differ based on the printing techniques and materials used. While some AM methods may not need any post-processing, others require extensive and careful treatment. For instance, components made from photosensitive resins via stereolithography (SLA) must undergo a post-curing process in a UV environment before the final application. Support structures are often necessary for parts with unsupported regions; printing without them can lead to layer dropouts. If support structures are employed, they must be removed afterwards. This can be done mechanically by cutting

them away or chemically by dissolving them in a solvent that does not damage the main part. [21]

In Figure 6, the main AM steps are graphically summarized: CAD, slicing, printing, and post-processing.

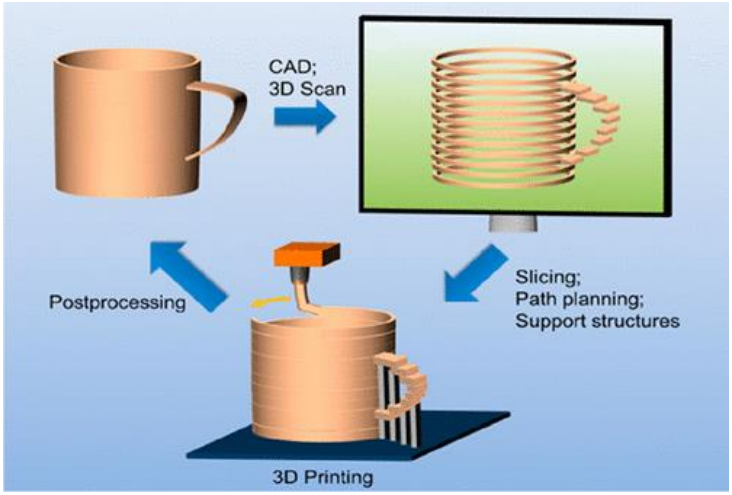

Figure 6. Basic principles of AM processes. [22]

2.2. CATEGORIES OF ADDITIVE MANUFACTURING

According to the ISO/ASTM 52900 standard [23], additive manufacturing processes are classified into seven categories:

1. Directed energy deposition (DED).
2. Material extrusion (MEX);
3. Material jetting (MJ);
4. Binder jetting (BJ);
5. Powder bed fusion (PBF);
6. Sheet lamination;
7. Vat photopolymerization (VP).

Nevertheless, the most commonly used techniques for 3D- printing of polymer composites are MEX, PBF, MJ and VP.

2.2.1. Material extrusion

MEX is a group of AM processes in which a polymeric material, mainly thermoplastics, is selectively applied layer by layer through extrusion from a nozzle. The most widely recognized technology within this category is Fused Filament Fabrication (FFF). This process utilizes the extrusion of a filament, which is a polymeric material typically wound onto a spool with diameters of 1.75 mm, 2.85 mm, or 3.00 mm. The filament is loaded into the extruder, where it is heated to a fused state and then extruded onto the build surface, solidifying rapidly to create a solid structure. The temperature of the printhead typically ranges from 190 to 280°C. The selection of nozzle diameter, generally between 0.4 and 0.6 mm for polymer composites, is determined by the material and the required print quality. In most FFF printers, the printhead moves along the X and Y axes while the build plate adjusts along the Z-axis. After each layer is applied, the build plate is lowered, allowing for the extrusion of the next layer, a process that continues until the entire model is completed. [24]

A schematic illustration of this process is shown in Figure 7.

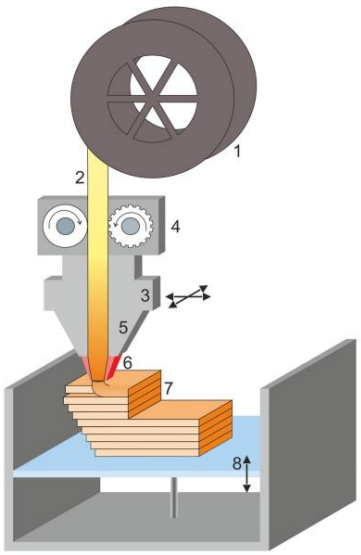

Figure 7. Schematic illustration of the material extrusion. (1) spooled material storage, (2) thermoplastic filament, (3) horizontally movable, heated deposition unit consisting of (4) counter-rotating driving wheels, (5) a liquefier, (6) a nozzle, (7) structural element fabricated in a layer-by-layer manner, and (8) vertically movable build platform. [25]

2.2.2. Powder bed fusion

PBF involves the selective fusion of powder using thermal energy [23]. Initially developed with Selective Laser Sintering (SLS), PBF has since evolved into various techniques that share similar working principles but differ in their binding mechanisms. [26] Unlike traditional fusion, powder particles are combined by melting. The process begins with a thin layer of powder, typically 0.1 mm thick, being deposited onto a platform. A laser beam then selectively sinters the powder, scanning the surface. Once the layer is complete, the platform lowers, and a new layer of powder is applied for selective sintering. This process is repeated layer by layer until the final product is formed. Since the powder bed itself provides support for the part, no additional support structures are needed, regardless of the complexity of the design. [24]

A schematic representation of this process is presented in Figure 8.

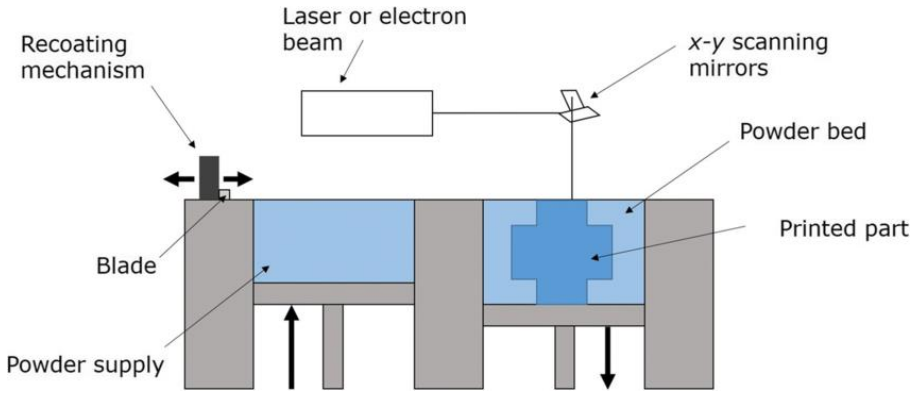

Figure 8. A schematic PBF process.[27]

2.2.3. Material jetting

MJ is the process of creating a model using droplets of liquid materials like photopolymer resin or wax. These materials are selectively deposited onto the work platform through a nozzle and solidified immediately after application. The model is formed layer by layer as the build platform lowers along the Z-axis. For polymers, UV light from a lamp integrated into the printhead is used to cure the material. [24]

Figure 9 provides a diagrammatic representation of this process.

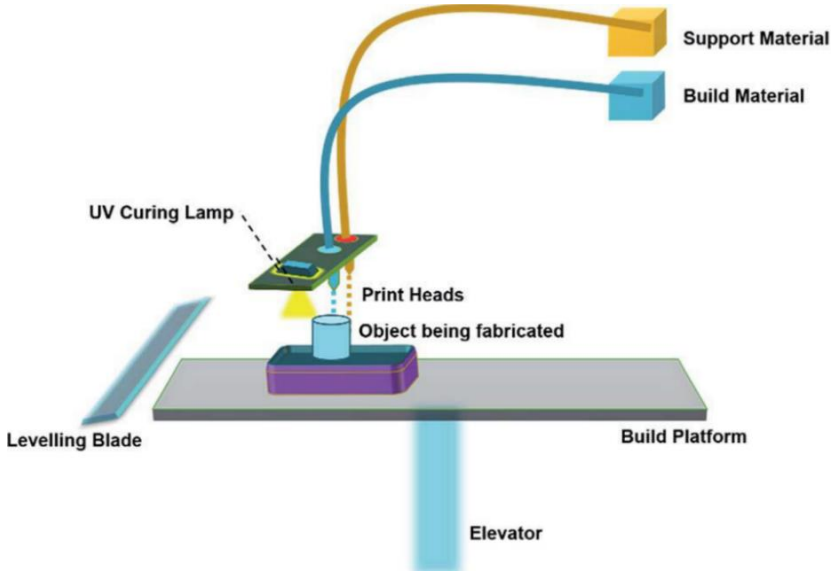

Figure 9. A schematic representation of MJ. [28]

2.2.4. Vat polymerisation

Vat Polymerisation (VP) is defined as an AM process in which a liquid photopolymer in a vat is selectively cured by light-activated polymerisation. [29]

Among additive manufacturing methods, VP offers the highest printing resolution and object complexity. However, its use is limited by the scarcity of sustainable photopolymer resins. Most commercially available 3D-printable photopolymers are based on fossil fuel-derived acrylates and epoxides. Growing environmental concerns and the depletion of fossil fuel resources are driving research toward developing greener alternatives. [30]

2.2.4.1. Photopolymers and photopolymerisation

A photopolymer is a light-curable resin that undergoes physical or chemical changes when exposed to either visible or UV light. The liquid resin, composed of elements such as liquid monomers, photo-initiators (PIs), reactive diluents, and oligomers, alters its properties upon light exposure. When curing occurs, PIs release reactive species that act as catalysts for chain formation among monomers and oligomers. This chain-forming process is irreversible, meaning prototypes cannot revert to their liquid form. This describes the photopolymerisation process. Utilizing this principle, consecutive layers of resin are gradually fabricated from a sliced STL file. [29], [31]

The principle of a typical photopolymerisation process is schematically provided in Figure 10.

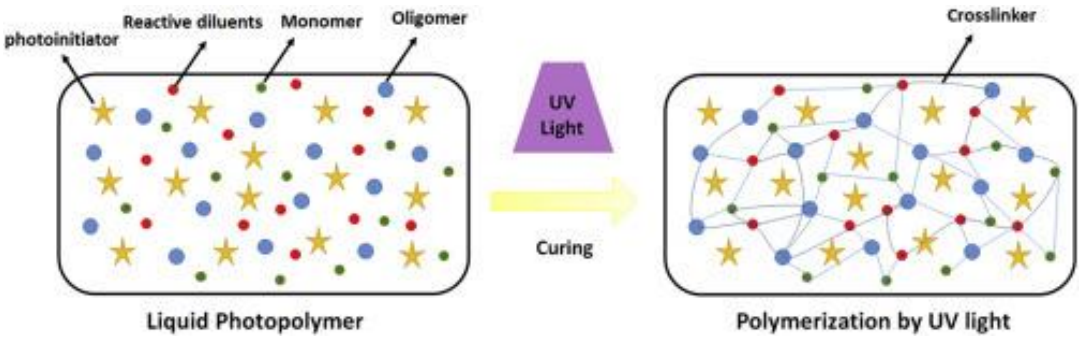

Figure 10. Schematic photopolymerisation process. [29]

Photoinduced processes can be divided into two main categories based on their mechanism: free-radical and ionic systems. [32]

These systems differ by the reactive species produced by PI when exposed to light. Both free radical and ionic processes involve three steps, as shown in Figure 11:

1. Initiation;
2. Propagation;
3. Termination.

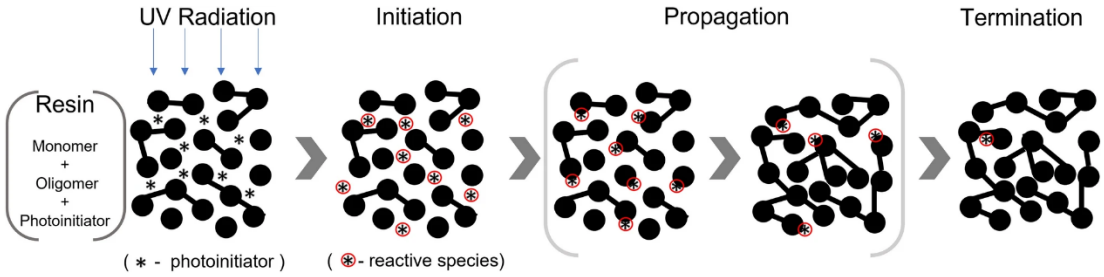

Figure 11. Schematic of the polymerisation process of a photosensitive resin. [20]

Initiation begins with the absorption of UV radiation by the PI, generating reactive species that react with oligomers and monomers to form long chains during propagation. Termination occurs through recombination, disproportionation, or occlusion.

In free radical polymerisation, free radicals can crosslink monomers like acrylates and styrene, unsaturated polyesters or thiol-ene and this process is fast, stopping once the light is removed. In contrast, ionic polymerisation, particularly cationic one, requires more

exposure time but continues even after the light source is removed. It is used for monomers such as ketones and aldehydes, epoxides, which do not polymerise via free radicals. [20]

As shown in many studies, radical photopolymerisation is especially effective at reacting with acrylate monomers in inert environments, which are also found in AESO. [32]

2.2.4.2. Free-radical photopolymerisation

In these photoinitiating systems, free radicals are generated from the photoinitiator (PI) after exposure to light radiation. Unimolecular (Type I) and bimolecular (Type II) photoinitiators are two types of compounds used to produce free radicals, each with distinct mechanisms. Type I PIs undergo homolytic bond cleavage upon absorbing a photon, resulting in the generation of two free radicals. In contrast, Type II PIs generate free radicals by abstracting hydrogen or electrons from co-initiator species after being excited to their triplet state by UV radiation. [20][33]

Commonly used commercial PIs are typically Type I, such as 2,4,6-trimethylbenzoyldiphenyl phosphine oxide (TPO) and phenylbis(2,4,6-trimethylbenzoyl) phosphine oxide (BAPO). These PIs have been widely utilized in VAT polymerisation processes with both UV light and 405 nm LEDs.

3. VAT POLYMERISATION TECHNIQUES

The vat polymerisation AM approach is categorized into different technologies depending on the type of light source used in the printer: stereolithography (SLA), direct light processing (DLP), and liquid crystal display-based (LCD) printers, also called daylight polymer printing (DPP). [18][34] Moreover, Continuous liquid interface (CLIP) is considered a vat-polymerization technology as it is a DLP variation. [34]

3.1. STEREOLITHOGRAPHY (SLA)

In the SLA, a building platform is submerged into a liquid photocurable polymer resin which is polymerised using ultraviolet (UV) light which traces the designated areas based on the sliced STL file, curing the resin layer by layer. After each layer is formed, the platform moves either up or down along the Z-axis, depending on whether the printer uses a top-down or bottom-up configuration, by an amount equal to the thickness of the layer. This process is repeated until the 3D object is fully constructed. Layer heights typically range between 12 and 150 µm, with 100 µm being the most selected. Standard SLA printers achieve a print speed of 10–20 mm/h. The precision of the SLA process is determined by the laser beam's spot size and is usually more than 100 µm. [31] The working principle of SLA is shown in Figure 12.

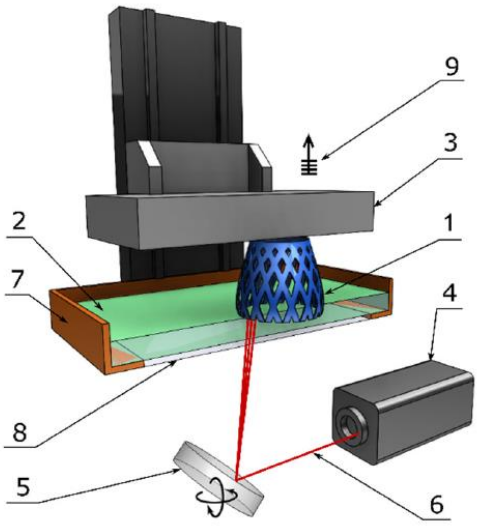

Figure 12. Components of a typical SLA machine: (1) printed part, (2) liquid resin, (3) building platform, (4) UV laser source, (5) XY scanning mirror, (6) laser beam, (7) resin tank, (8) window, and (9) layer-by-layer elevation. [31]

3.2. DIGITAL LIGHT PROCESSING (DLP)

In DLP printers, the polymer is exposed to light using a projector or a digital micromirror device (DMD), which projects a mask of light that cures the entire layer simultaneously, as visible in Figure 13. This differs from SLA technology, where a mirror reflects a laser source to cure the resin. As a result, DLP is faster because it cures the whole layer at once. However, since it uses a digital light projector, the layers are pixelated, and the precision of the printed object depends largely on the resolution of the projector. [31]

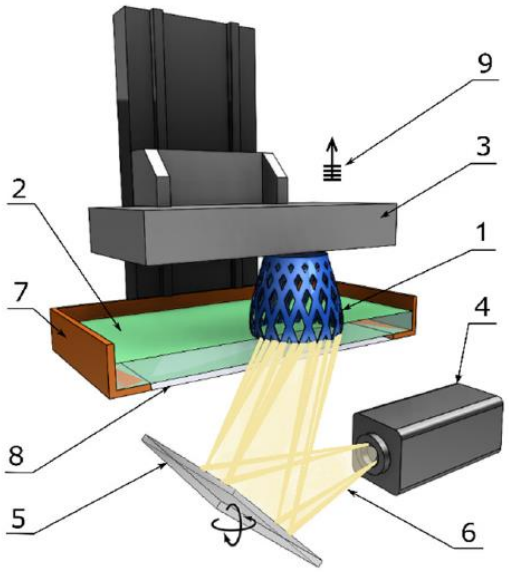

Figure 13. Components of a typical DLP machine: (1) printed part, (2) liquid resin, (3) building platform, (4) light source, (5) digital projector, (6) light beam, (7) resin tank, (8) window, and (9) layer-by-layer elevation. [31]

3.3. CONTINUOUS LIQUID INTERFACE (CLIP)

CLIP technology is an advancement of DLP technology. It uses digital projection with LEDs and an oxygen-permeable window, which creates a thin "dead zone" near the window. This dead zone is essential because one of the major challenges of free radical photopolymerisation is its sensitivity to oxygen. Oxygen inhibits the curing process by reacting with free radicals and preventing them from initiating polymerisation. As a result, the dead zone allows uncured resin to flow freely, enhancing print resolution and reducing the risk of layer separation failures. Additionally, unlike traditional SLA and DLP technologies, CLIP machines enable continuous movement of the build platform, allowing uninterrupted printing at speeds of several hundred millimetres per hour. This method eliminates layer adhesion issues and minimizes the staircase effect, resulting in parts with isotropic mechanical properties. [31]

As in DLP, the resolution is determined by the pixel size of the projector. [34]

A representation of this process is shown in Figure 14.

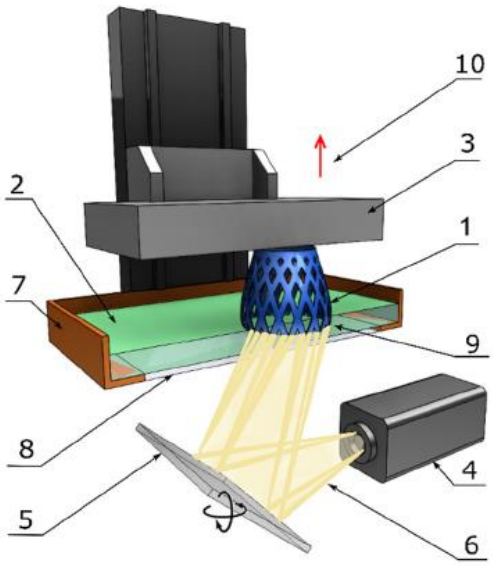

Figure 14. Components of a typical CLIP machine: (1) printed part, (2) liquid resin, (3) building platform, (4) light source, (5) digital projector, (6) light beam, (7) resin tank, (8) oxygen-permeable window, (9) dead zone, and (10) continuous elevation. [31]

3.4. LIQUID CRYSTAL DISPLAY (LCD)

The high cost of traditional 3D printing equipment can limit engineering applications and research opportunities. In contrast, LCD 3D printing technology offers an emerging method for UV curing photosensitive resin, combining high precision with fast printing speeds.
The main differences between these vat polymerisation techniques are based on their light curing system and the costs involved.

- SLA uses a laser to trace the cross-section of each layer onto the surface of the resin. This method is highly precise and can produce intricate details, but it is relatively slow because the laser must cure the resin point by point. Additionally, the need for specialized light-guiding components contributes to higher costs and makes SLA less efficient for large-scale printing. [35]
- In contrast, DLP projects the entire image of a layer all at once using a digital light projector. This significantly speeds up the process compared to SLA since each layer is cured simultaneously. DLP offers a good balance between speed and resolution, but like SLA, it requires costly projection systems. [35]
- LCD technology, conversely, enhances the printing process by utilizing an LCD screen to control the light transmission, curing the resin only where necessary. This approach eliminates the need for expensive light-guiding systems, making these printers more affordable. Additionally, LCD combines fast printing speeds with precision, like DLP, while maintaining lower operational costs. However, a significant limitation is the durability of the LCD screen, which may degrade with prolonged exposure to UV light. [36]

The operational principle of an LCD printer, shown in Figure 15, involves a computer program that sends image signals to the LCD, creating specific transparent regions for UV light to pass through and cure the resin in the vat. After each layer is cured, the platform elevates to replenish the resin and then descends to expose and cure the next layer.

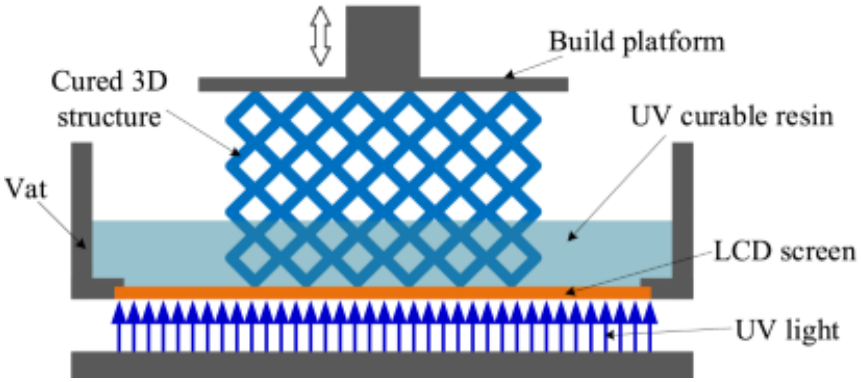

Figure 15. Working principle of the LCD-type 3D printer. [36]

Overall, this technology presents significant potential for broader engineering applications in 3D printing, thanks to its cost-effectiveness, speed, and ability to fabricate intricate 3D objects layer by layer.

In the following experimental work, an LCD printer was chosen for the manufacturing of AESO-based photosensitive resin filled with biochar, where the photopolymerisation is induced by accounting for light heterogeneity, low irradiance, and a 405 nm illumination wavelength.

4. MATERIALS AND METHODS

In this chapter, a detailed discussion of the materials and methods used in the experimental work follows.

4.1. MATERIALS

4.1.1. Acrylate Epoxidized Soybean Oil (AESO)

Vegetable oils (VOs) represent a sustainable resource with significant potential for the synthesis of polymer materials due to their renewable nature, abundant availability, and simple chemical modification. Currently, VOs play a key role as a raw material that integrates biomass with 3D printing technology and have been extensively studied for photo-curing 3DP applications. [37]

Structurally, they are triglycerides composed of three fatty acids joined together to a glycerol unit. One of the most produced VOs is soybean oil, extracted from soybean seeds. [30] Through a process that begins with epoxidation and is followed by acrylation, the unreactive double bonds in soy oil are functionalized with acrylate groups, enabling free-radical polymerisation. [38] This results in the formation of AESO (Figure 16).

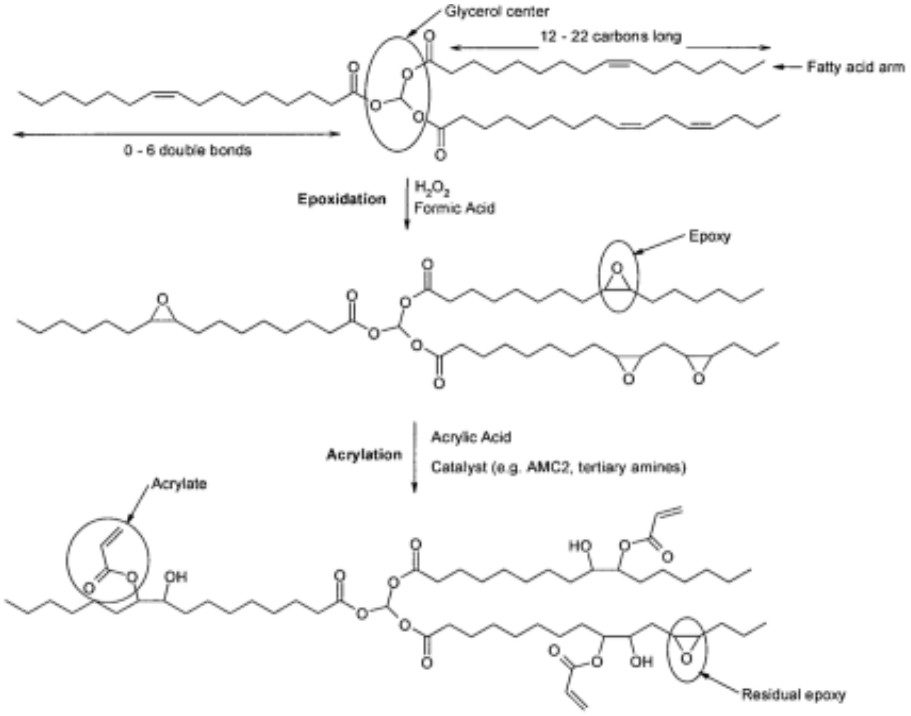

Figure 16. Chemical structure of AESO after epoxidation and acrylation of soybean oil. [38]

In this study, acrylate epoxidized soybean oil was purchased from Merck. At room temperature, as shown in Figure 17, it appears as a viscous liquid with a colour ranging from yellow to amber and with a density of 1.04 g/ml. [39]

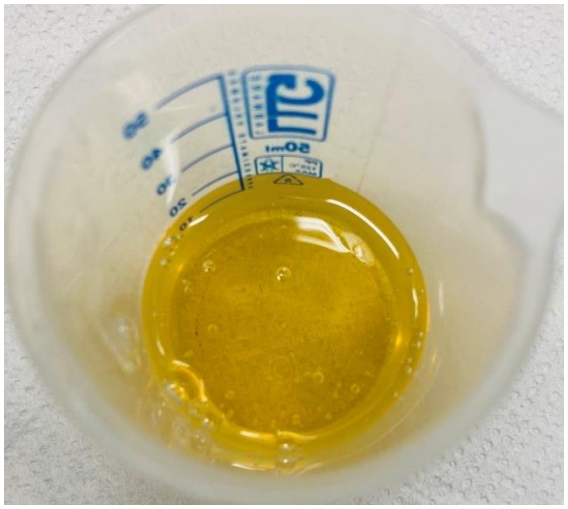

Figure 17. AESO appearance as purchased from Merck.

4.1.2. Isobornyl methacrylate (IBOMA)

The prototyping of pure AESO is difficult and time-consuming due to its high viscosity, reported to be between 15000 and 38000 cP at 25°C. [39] However, the viscosity of AESO could be reduced by adding reactive diluents (RDs), which actively participate in the cross-linking reaction. [7] Synthetic RDs are widely used. However, they are neither bio-based or biodegradable. [7] Several studies have suggested the use of bio-based diluents, such as isobornyl methacrylate (IBOMA), as a valid alternative to conventional RDs.

IBOMA, whose chemical structure is shown in Figure 18, is the monofunctional bio-based reactive diluent, derived from pine sap, selected for this experimental work. [7]

It was purchased from Merck and has a density of 0.983 g/mL at 25 °C. This transparent liquid possesses a viscosity of 10–15 cP and a glass transition temperature of 170 °C. [40]

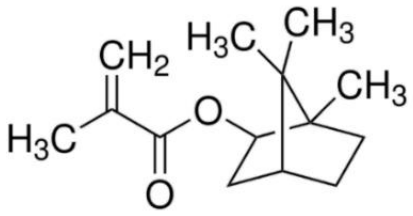

Figure 18. Chemical structure of IBOMA. [40]

4.1.3. Phenylbis (2,4,6-trimethylbenzoyl) phosphine oxide (BAPO)

Phenylbis (2,4,6-trimethylbenzoyl) phosphine oxide (BAPO) was chosen as a type I photoinitiator [41], and its chemical structure is shown in Figure 19.

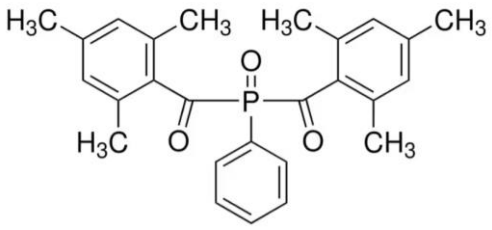

Figure 19. Chemical structure of BAPO. [42]

The UV/Vis spectrum of BAPO exhibits the highest absorbance peak around 295 nm. [43] Among the most used photoinitiators depicted in Figure 20, such as TPO, TPOL, and DMPA, BAPO has the broadest absorption spectrum at 405 nm, which is the wavelength emitted by the LCD printer utilized.

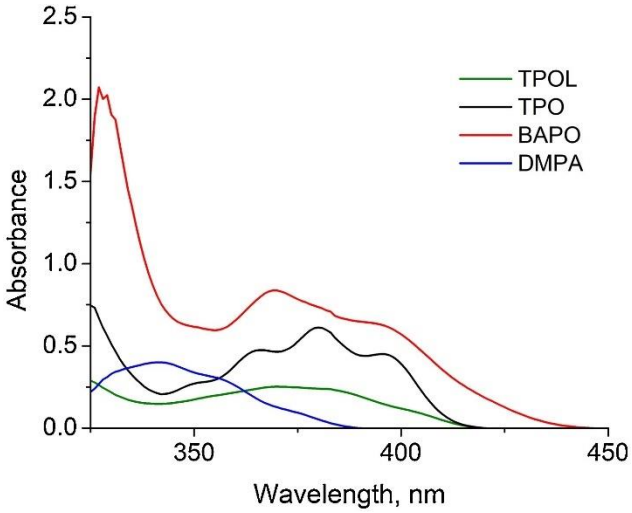

Figure 20. UV/Vis spectrum of TPOL, TPO, BAPO, DMPA. [43]

It was purchased from Merck and appears as a crystalline powder ranging in colour from white to yellow (Figure 21). [42]

Figure 21. BAPO appearance as purchased from Merck.

4.1.4. Biochar

Polymers are modified through the addition of various fillers, allowing them to evolve into composites and extending their range of applications in electronics, mechanics, and biomedical industry. [9]

The increasing global population, combined with technological advancements and economic progress, has led to a significant increase in the demand for fossil fuels, resulting in considerable environmental pollution and depletion of natural resources. [44]

Concurrently, the heightened need for food has resulted in a considerable accumulation of agricultural waste. Traditional disposal methods, such as incineration and landfilling, not only contribute to air and water pollution but also worsen the greenhouse effect, posing serious threats to both food security and environmental health. Thus, finding effective strategies for managing agricultural waste is essential. [44]

Recently, the synthesis of carbon from sustainable biomass-based precursor materials, often known as *biochar*, has attracted the interest of researchers all around the world. [45]

Biochar is a carbon-rich product generated from thermochemical pyrolysis from 400 to 900-1000 °C of biomass materials in an inert environment [46] and can be produced from almost any organic source.

It has emerged as a viable alternative to other high-cost carbon fillers due to its capacity to enhance the mechanical, electrical, and thermal properties of the final product. The performance of biochar appears to be influenced by two main parameters: the *feedstocks* and the *pyrolysis temperature*. [47]

4.1.4.1. Biochar feedstocks

The *feedstocks* are generally categorized into *lignocellulosic* and *non-lignocellulosic* biomass, each yielding biochar with distinct physicochemical characteristics. [48]

Wastes and residues from *lignocellulosic* biomass currently have limited and low-value applications, making them widely available for biochar production. Common sources of lignocellulosic biomass include agricultural and forestry residues, which are rich in primary constituents such as lignin, cellulose, hemicellulose, extractives, and trace amounts of inorganic compounds. The proportions of these components can vary significantly depending on the source of the biomass. Notably, biomass with a lower inorganic content tends to yield biochar with reduced ash levels. Consequently, lignocellulosic biomass has been extensively utilized for synthesizing pyrolytic biochar. [48]

In contrast, *non-lignocellulosic* feedstocks, such as sewage sludge and livestock-derived biomass, contain a more complex mixture of proteins, lipids, saccharides, minerals, and other components. This complexity leads to intricate thermochemical reactions during pyrolysis, often resulting in biochar with less favourable properties, including lower carbon content and higher ash content compared to that derived from lignocellulosic sources. High ash content in biochar can adversely impact the reinforcing properties of composite materials. [48]

4.1.4.2. Pyrolysis temperature

During the production process, pyrolysis parameters, particularly temperature, play a crucial role in influencing both the yield and the characteristics of the final product. Lower pyrolysis temperatures tend to produce higher biochar yields along with increased emissions of volatile compounds during heat treatment and excellent cation-exchange capacity. Conversely, treatments at higher temperatures generate activated biochar with a greater proportion of aromatic carbon, enhanced alkalinity, a larger specific surface area, and increased microporosity. [47]

Cellulose is the primary component of lignocellulosic biomass and serves as one of the most widely utilized feedstocks in biorefinery platforms and processes. [49]

The biochar used in this experimental work has been defined as having a shape of “defective spheres” [49] and was provided by a research group from the Politecnico di

Torino, which produced it via pyrolysis of crystalline nanocellulose (CNC) at a temperature of 400 °C, with a heating rate of 10°C/min, maintained at the maximum temperature for 30 minutes. The entire process took place in a nitrogen atmosphere. [49], [50]

A representative image of the biochar from a macroscopic perspective is displayed in Figure 22.

Figure 22. Biochar from pyrolysis at 400°C of CNC.

4.2. METHODS

4.2.1. Preparation of resin for LCD 3D Printing

Various photocurable formulations were prepared by mixing AESO with the IBOMA diluent in a 50/50 w ratio to achieve the desired resin viscosity, lower than 800-1000 cP as required for LCD printing technology. [7]

BAPO was added at a concentration of 2 phr across all samples. Consequently, biochar was incorporated at 0.5, 1, and 2 parts per hundred resin (phr).

To designate each formulation were used acronyms, as detailed in the following Table 1.

Table 1. Description of the formulations and associated acronyms.

Acronyms	Formulations
A-IB	AESO+IBOMA (50/50 %w/w) + 2 phr BAPO
A-IB+BC0.5	AESO+IBOMA (50/50 %w/w) + 2 phr BAPO + 0.5 phr BIOCHAR
A-IB+BC1	AESO+IBOMA (50/50 %w/w) + 2 phr BAPO + 1 phr BIOCHAR
A-IB+BC2	AESO+IBOMA (50/50 %w/w) + 2 phr BAPO + 2 phr BIOCHAR

To prepare the photocurable formulations, equal amounts of AESO and IBOMA were mixed by magnetic stirring for 2 hours at room temperature (RT). Then, 2 phr of BAPO photoinitiator was added to the mixture, which was stirred again for 30 minutes at RT. Finally, to obtain a more homogeneous solution and to improve the dispersion of the BAPO, the formulation was treated using an ultrasonic bath for 15 minutes at 60 °C, yielding the AESO-based resin.

For the preparation of the composite materials, the biochar was first dried in an oven at 100 °C overnight to prevent moisture absorption.

Subsequently, the appropriate amount of carbonaceous filler was added to the AESO-IBOMA formulations to achieve concentrations ranging from 0.5 up to 2 phr. To ensure uniform dispersion and disentanglement of the biochar, the mixtures were homogenized using an Ultra-Turrax T 10 basic for 3 minutes at power level 4 out of 6. This was followed by additional homogenization in an ultrasonic bath at 60 °C for 15 minutes. Once fully dissolved, the formulations were stored in a dark environment to prevent premature curing due to light exposure [32] and were kept in the same dark environment during the printer setup, before being subjected to the printing process.

4.2.2. Sedimentation tests

After preparing the formulations, sedimentation tests were conducted. These tests are essential for evaluating whether the mixture can maintain its characteristics over time by analysing the stability of the dispersed bio-filler particles. If the filler tends to sediment or separate quickly, it indicates poor dispersion stability which can lead to printing defects, as the filler is not uniformly distributed. Additionally, this can result in variations in the mechanical properties of the produced composites.

The sedimentation test was performed on each formulation containing biochar at intervals of 1, 2, 3, 4, 5, 6, 7, 8, and 24 hours, allowing for continuous monitoring of the mixture's behaviour over time.

Due to the black colour of the biochar, and consequently, of the formulation in which it is dispersed, sedimentation was not visually observed for more than 8 hours, as seen in Figure 23.

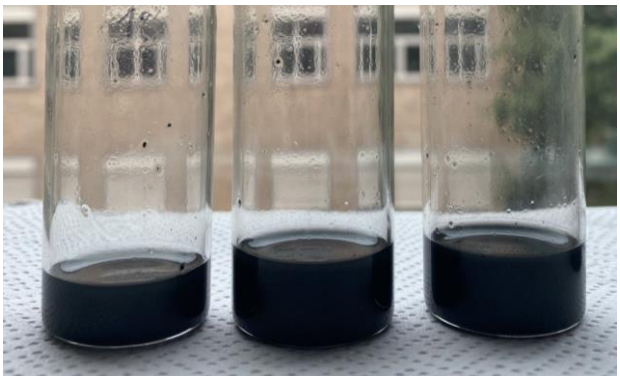

Figure 23. Sedimentation test after 8h for formulations containing 0.5, 1, and 2 phr of BC.

However, after 24 hours, a deposit of biochar was noticed, primarily in the cases where it was dispersed at concentrations of 1 and 2 phr, as shown in Figures 24 and 25, respectively.

Figure 24. A-IB+BC1 after 24 h.

Figure 25. A-IB+BC2 after 24h.

4.2.3. 3D printing and post-curing

After preparing the liquid photocurable formulations, the resins were 3D printed using an LCD Phrozen Sonic Mini 8K printer. This utilizes a 50 W linear projection LED module as its light source, providing an XY resolution of 22 µm (1152 PPI) and operates at a UV wavelength of 405 nm.

The Phrozen Sonic Mini 8K, shown in Figure 26, is compact, with dimensions of 29 cm (L) x 29 cm (W) x 43 cm (H) and a weight of 13 kg, making it suitable for research applications. It offers a printing volume of 16.5 cm (L) x 7.2 cm (W) x 18 cm (H) with layer thickness (Z resolution) adjustable from 0.01 to 0.30 mm. Furthermore, its small resin vat allows for minimal resin usage, enabling effective printing tests without excessive preparation or material waste.

Figure 26. Phrozen Sonic Mini 8K.

For the slicing step, Phrozen offers CHITUBOX V1.9.0 or above, allowing users to load STL files. The software provides various options for selecting piece orientation and adjusting printing parameters, such as support size and shape, exposure time, layer thickness, and platform velocity, as shown in Figure 27 which illustrates a parameter configuration window in Chitubox.

Figure 27. Chitubox window for adjusting printing parameters.

To identify the optimal printing parameters, a comprehensive testing procedure was performed for each formulation. Initially, the printability of the AESO-based formulation was assessed, starting from printing parameters derived from previous literature on similar resins. Subsequently, a systematic optimization of the relevant settings for the preparation of the composite formulations was carried out.

The printing details for each formulation are presented in Table 2.

Table 2. Printing parameters for each photocurable formulation.

Printing parameters	A-IB	A-IB+BC0.5	A-IB+BC1	A-IB+BC2
Layer height (mm)	0.1	0.1	0.1	0.1
Exposure time (s)	15	18	22	40
Bottom exposure time (s)	18	20	30	45
Rest time before lift (s)	0	0	0	0
Rest time after lift (s)	0	0	0	0
Rest time after retract (s)	4	4	4	4
Bottom lift distance (mm)	4	4	4	4
Lifting distance (mm)	4	4	4	4
Bottom lift speed (mm/min)	80	80	80	80
Lifting speed (mm/min)	80	80	80	80
Bottom retract speed (mm/min)	80	80	160	160
Retract speed (mm/min)	80	80	160	160

After printing, the parts were removed from the platform and cleaned for fifteen minutes using 1-butanol (purity > 99.4%) from Merck as a washing solvent. The components were then left to air-dry for 24 hours. Finally, they underwent post-curing for one hour in the Anycubic Wash & Cure Plus, represented in Figure 28.

Figure 28. Anycubic Wash & Cure Plus by Anycubic.

The Anycubic Wash & Cure Plus measures 290 mm in length, 270 mm in width, and 479 mm in height, with a weight of 6.5 kg. It features LED lights operating at a wavelength of 405 nm and has a maximum power output of 40 W. [51]

4.3. CHARACTERIZATION TESTS

Several characterization tests have been conducted on the biochar powders as well as on the photocurable formulations and the printed samples, including both cured and uncured, filled with BC and unfilled.

4.3.1. Rheological analysis

To determine the best formulation for 3D printing, several samples were prepared by mixing AESO with IBOMA in different ratios ranging from 70:30 to 30:70 in weight percentage (%w/w), along with 2 phr of BAPO and biochar in amounts varying from 0.5 to 2 phr. After the viscosity tests, the A-IB composition was selected, as it provided the appropriate viscosity values for LCD printing. [7]

Viscosity is a key property of resin used in LCD 3D printing, as it measures the resistance of the resin to flow and affects how easily it can be manipulated during the printing process.

In these formulations, viscosity was measured at room temperature using an Anton Paar MCR 302 Modular Compact Rheometer (Graz, Austria), configured in a parallel plate setup, as illustrated in Figure 29.

Figure 29. Anton Paar MCR 302 Modular Compact Rheometer (Graz, Austria).

Measurements were conducted across a shear range from 0.1 Hz to 1000 Hz, and the output dynamic viscosity was recorded in mPa·s. A water circulation system maintained the temperature at 25 °C, while the measuring gap was set to 0.200 mm.

4.3.2. Gel content percentage

The insoluble fraction, or gel content, of the photocured samples, was measured following the ASTM D2765-16 standard. Specifically, the specimens were first weighed before immersion in chloroform for 24 hours, ensuring complete submersion. After extraction, the samples were dried overnight at 80°C in an oven to remove any residual solvent and then weighed again. [52]

The percentage of gel content (G%) reflects the degree of crosslinking in the polymer and is calculated according to Eq. (1):

$$G\% = \left(1 - \frac{w_i - w_f}{w_i}\right) \cdot 100 \qquad \text{Eq. (1)}$$

Where w_i is the initial weight of the samples and w_f is the final weight after treatment with chloroform and drying.

4.3.3. Thermogravimetric analysis

The thermal stability of the 3D samples was assessed through thermogravimetric analysis (TGA). This method involves monitoring the sample's mass change as a function of temperature, or time, under controlled conditions. The TGA apparatus consists of a highly sensitive analytical balance with an alumina crucible to hold the sample, which is heated externally. The analysis can be conducted in either an inert atmosphere (N_2 or Ar) or an oxidizing atmosphere (air). The heating rate can be kept constant, and the mass variation is continuously recorded. A connected computer tracks these changes and generates a graph, with the x-axis representing time or temperature, and the y-axis showing the sample's weight in milligrams. [53]

The analysis was conducted using a Mettler-Toledo TGA 851e instrument (Columbus, OH, USA), represented in Figure 30, over a temperature range of 25 to 900 °C, with a heating rate of 10 °C/min and an airflow of 50 ml/min. The TG curves were normalized to the unit mass of the samples and the DTG curves were derived from the respective thermograms. [54]

Figure 30. Mettler-Toledo TGA 851e instrument.

4.3.4. Differential scanning calorimetry

Differential scanning calorimetry (DSC) is a widely utilized thermal analysis technique that explores the thermal behaviour of polymeric materials, allowing for the identification of key thermal characteristics, including melting point (Tm), crystallization temperature (Tc), and glass transition temperature (Tg). These properties are displayed as distinct peaks or shifts in the resulting heat flow curve, commonly known as the thermogram. In this method, a test sample is compared with a reference material, which has well-known thermal properties. [55] Both samples are maintained at the same temperature and subjected to gradual heating or cooling at a constant rate, while the difference in heat flow is measured. [54] The term "differential" reflects this comparative analysis.

In the present study, DSC was used to determine the Tg values of the cured thermoset polymeric material, which is fully amorphous. Due to the absence of crystalline domains, no melting or crystallization peaks were detected. The measurements were performed using a DSC 214 Polyma instrument (Selb, Germany), depicted in Figure 31. The analysis covered a temperature range of -50 to 250 °C under a nitrogen atmosphere with a flow rate of 40 ml/min, maintaining both heating and cooling rates at a constant 10 °C/min. The experimental procedure involved two heating scans, the first of which was specifically designed to erase the thermal history of the polymer, followed by a cooling scan.

Figure 31. DSC Polyma instrument (Selb, Germany).

4.3.5. Dynamic-mechanical thermal analysis

A complete viscoelastic characterization of photocured AESO-based materials was obtained through dynamic mechanical thermal analysis (DMTA). This technique measures the dynamic storage modulus (*E'*), the loss modulus (*E''*), and the damping factor (*tan δ*) as the temperature is varied. [56] [57]

The storage modulus (*E'*) represents the energy stored in the material, which is released after mechanical stress, and is a measure of the material's elasticity, or its ability to store energy. In contrast, the loss modulus (*E''*) reflects the material's capacity to dissipate energy as heat, indicating the viscous nature of the material.

When the storage modulus exceeds the loss modulus, the material behaves mainly elastically. Conversely, if the loss modulus is higher, the material is predominantly viscous. [56]

The damping factor, or *tan δ*, is the ratio between the loss and storage moduli and indicates the degree of energy dissipation. Furthermore, the peak of *tan δ* represents the midpoint between the glassy and rubbery state, so it can be defined as the Tg. [57] It is important to highlight that the glass transition temperature evaluated using DMTA could be distinct from that measured through DSC. Although both techniques relate to the same physical phenomenon, they provide different information and may yield slightly different Tg values due to the nature of their measurement methods.

DMTA measures the dynamic mechanical properties of a material, such as the storage and loss moduli, as temperature changes. The Tg is determined from the peak of tan δ, marking the transition from the glassy to the rubbery state, highlighting the material's viscoelastic behaviour and energy dissipation. On the other hand, DSC evaluates heat flow during phase transitions, with Tg detected as a step change in heat capacity. While both techniques detect the glass transition, DMTA emphasizes mechanical properties and viscoelastic behaviour, whereas DSC focuses on thermal properties, often resulting in slightly different Tg values between the two methods.

The DMTA tests were performed on unidirectional samples with dimensions of length of 35 mm, a width of 10 mm, and a thickness of 2 mm. Two examples of specimens used, one from A-IB resin and the other with the addition of 2 phr of biochar, are shown in Figures 32 and 33, respectively. [58]

Figure 32. A-IB DMTA specimen.

Figure 33. A-IB+BC2 DMTA specimen.

The test was conducted using an Anton Paar MCR 702e Multidrive (Graz, Austria) device (Figure 34), applying uniaxial sinusoidal stress with an amplitude of 1 N and a frequency of 1 Hz. The experiment was terminated once the material reached the rubbery plateau.

Figure 34. Anton Paar MCR 702e Multidrive (Graz, Austria).

4.3.6. Tensile tests

The tensile properties of the 3D printed samples were evaluated using dog bone-shaped specimens (type 5A) following the ISO 527-2 standard. Each specimen featured a gauge length of 26 mm, a width of 4 mm, and a thickness of 3 mm, ensuring standardized conditions for accurate testing. [59]

A representative example of a dog bone specimen derived from the resin with 2 phr of biochar is presented in Figure 35.

Figure 35. Dog bone specimen filled with biochar in 2phr.

The assessments were performed using an Instron 5966 machine, reported in Figure 36, equipped with a 2 kN load cell and pneumatic grips. Conducted at a deformation rate of 2 mm/min with a grip separation of 50 mm, this testing enables the measurement of various mechanical parameters, including tensile strength at break, elongation at break, and elastic modulus. These parameters are crucial for characterizing the resin from a mechanical perspective, and for exploring potential industrial applications of the material.

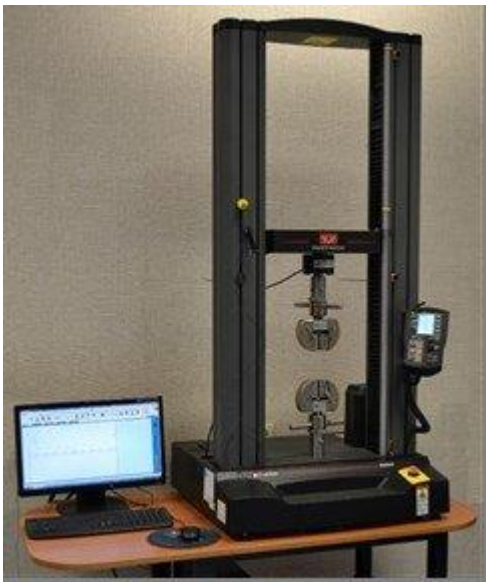

Figure 36. Instron 5966 tensile machine.

4.3.7. Morphological analysis: FESEM

Scanning electron microscopy (SEM) is a widely used technique that provides detailed images of a sample's surface by scanning it with a focused beam of primary electrons. When these electrons interact with the surface atoms, secondary electrons are emitted, which are detected to generate an image of the sample's topography. SEM also records backscattered electrons, which provide compositional information based on atomic density. SEM's resolution is influenced by factors such as the electron beam spot size and interaction volume, typically achieving resolutions down to 3 nm under optimal conditions. [60]

Field emission scanning electron microscopy (FESEM) is an advanced form of SEM that uses a field emission gun (FEG) to achieve higher resolution and improved image quality. In FESEM, a strong electric field near the tip of the filament in the gun produces a highly focused and stable beam of electrons. This design results in finer control over the electron

beam, reducing sample charging and enabling resolution as fine as 1 nm. FESEM's superior performance is driven by several key elements: a beam booster to maintain energy, precise electromagnetic apertures, and magnetic field lenses for enhanced beam focusing. These factors allow FESEM to excel in nanoscale imaging, making it particularly valuable for applications that require high precision and surface detail. [60]

FESEM has been effectively employed to analyse the morphology and dispersion of spheroidal biochar powders within the photocured samples, providing high-resolution images that reveal the distribution and interaction of the bio-filler within the polymeric matrix.

Each specimen was fractured using liquid nitrogen to preserve the internal structure and metallized with platinum using a Quorum Sputter Coater, model Q150T S (Laughton, East Sussex), for two cycles of 30 seconds to enhance surface conductivity. The fracture surfaces were then analysed using a ZEISS Merlin field-emission scanning electron microscope (FESEM) (Carl Zeiss Microscopy GmbH, Jena, Germany), as illustrated in Figure 37.

Figure 37. ZEISS Merlin field-emission scanning electron microscope (FESEM).

5. RESULTS AND DISCUSSION

This chapter outlines and analyses the results of the printing tests, as well as the characterizations performed on biochar powders, the formulated photocurable materials, and the resultant printed samples.

5.1 BIOCHAR POWDERS' CHARACTERIZATION

The Biochar powders were examined through FESEM analysis and TGA.

5.1.1. FESEM analysis

The results of the morphological analyses performed via FESEM on the biochar powders are shown in Figures 38, 39, and 40.

Figure 38 was captured at a magnitude of 1000x and shows the shape of the powders, described as defective spheres, or spheroidal.

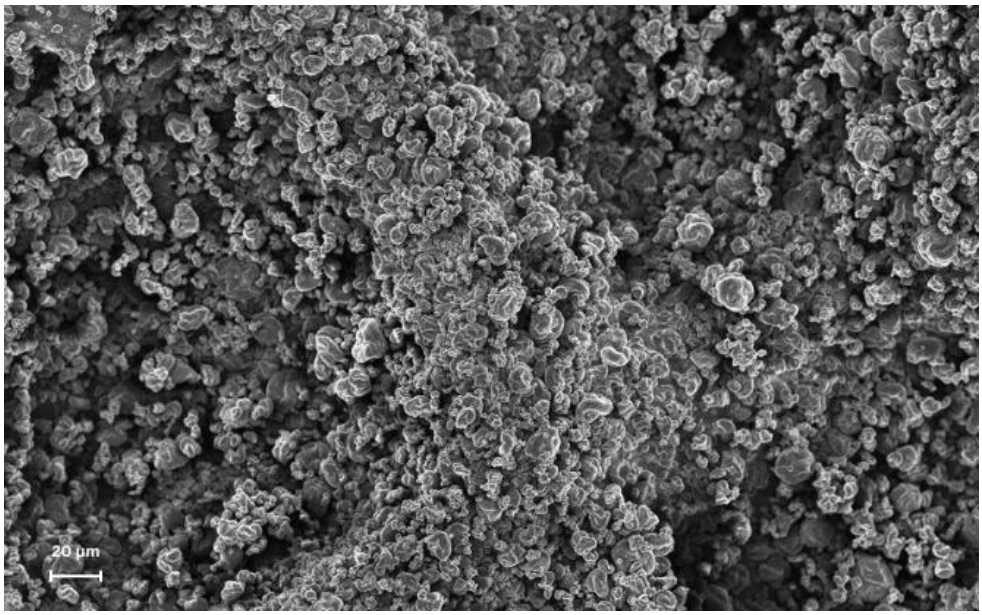

Figure 38. FESEM of Biochar powders at 1000x.

The image displays surface defects caused by the release of volatile organic compounds during pyrolysis. In the early stages of CNC thermal degradation, the surface of the spheres underwent pyrolysis while high-boiling compounds, such as levoglucosan, glucose dimers, and trimers, were released from the inner cores of the particles. As these compounds reached the surface, they simultaneously started to boil and decompose. This process

resulted in the formation of small bubbles, clearly visible in Figure 39, at 5000x, and further magnified in Figure 40, at 15000x. [49]

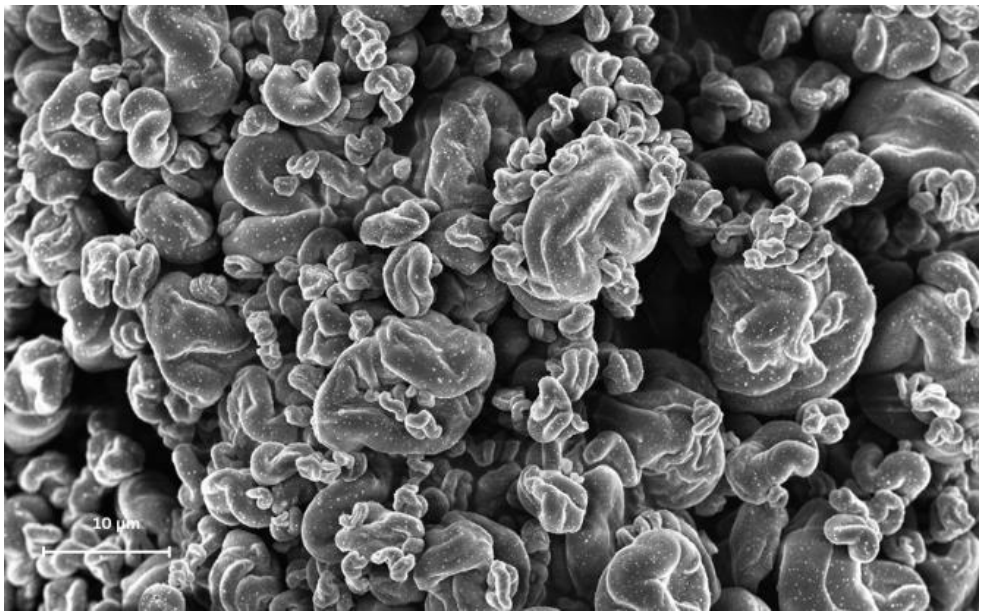

Figure 39. FESEM of Biochar powders at 5000x.

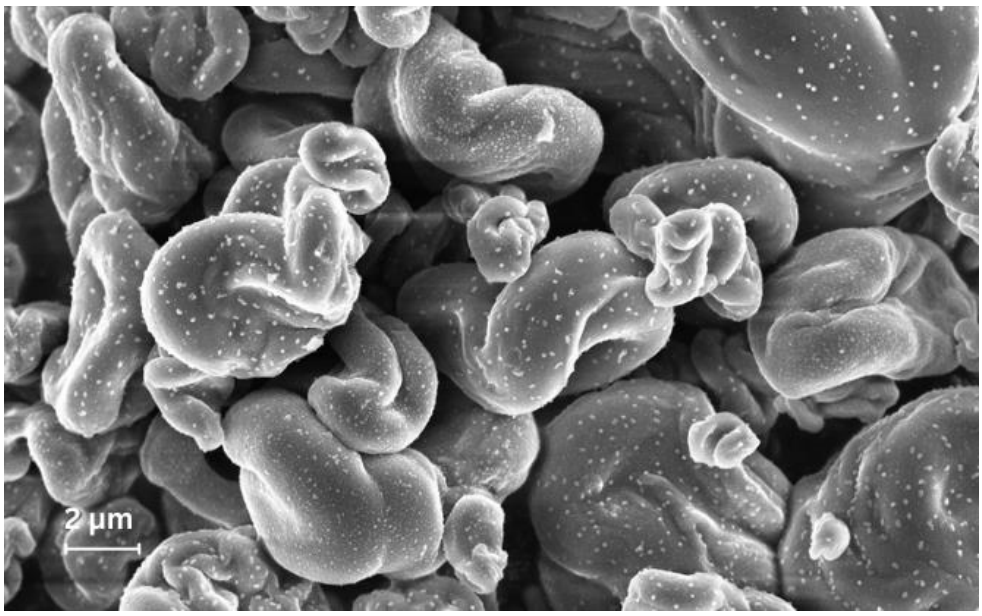

Figure 40. FESEM of Biochar powders at 15000x.

Additionally, the FESEM images provide an approximate estimate of the biochar particle sizes, which appear to range from slightly less than one micrometre to approximately 4-6 micrometres.

5.1.2. Thermogravimetric analysis on biochar powders

The thermogravimetric tests for the biochar powders are shown in Figure 41, which presents the thermogram in black and its first derivative in red.

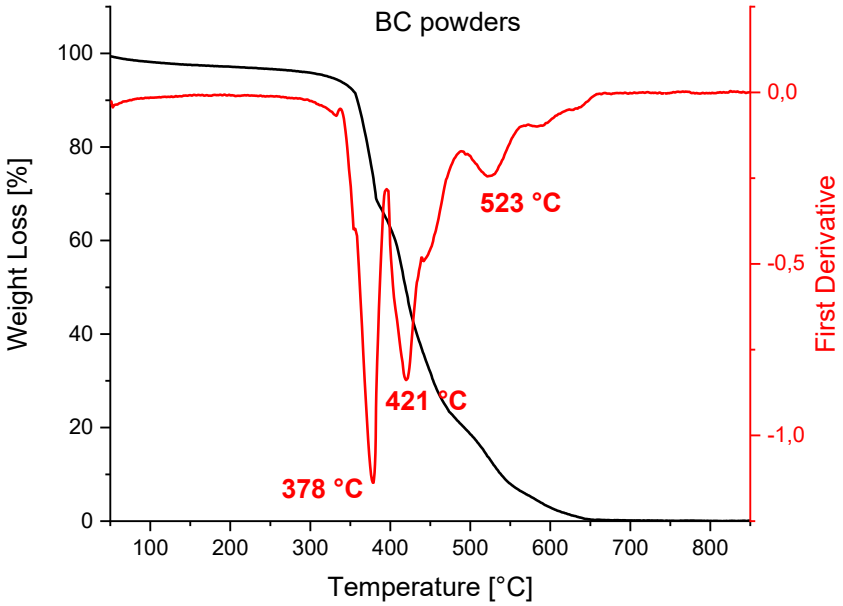

Figure 41. TGA of BC powders.

The experimental data indicate that an initial weight loss of 5% occurs at 323 °C, while at 421 °C, the sample has lost half of its weight, and at 523 °C, it has lost 90%. The peak of maximum degradation is observed at 378 °C, and no ash remains at the end of the analysis, indicating the absence of inorganic residues because cellulose does not contain inorganic components in its own composition. Furthermore, it highlights that the pyrolysis process was conducted optimally and left no impurities in the powders.

The most relevant results of the analysis are presented concisely in Table 3.

Table 3. Results of TGA on biochar powders.

Sample	T_{onset}*	$T_{degrmax}$	$T_{50\%}$	$T_{90\%}$	Ash
	[°C]	[°C]	[°C]	[°C]	[%]
BC powders	323	378	421	523	0

*T_{onset} is the temperature at which a weight loss of 5% occurs.

5.2. RHEOLOGICAL ASSESSMENT OF RESIN FORMULATIONS

The results of viscosity tests on the different printable formulations are shown in Figure 42. Increasing the biochar content in the formulations leads to a rise in viscosity, as also highlighted in Table 4, which provides the values at a shear rate of 10 s^{-1}.

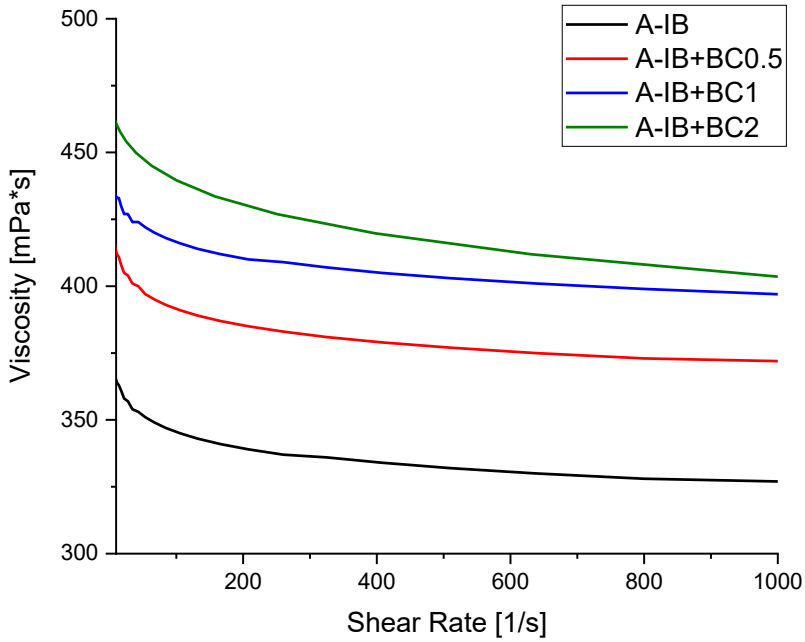

Figure 42. Comparison of shear rate-viscosity curves for different formulations.

For each formulation, a shear-thinning behaviour is observed, with viscosity decreasing as the shear rate increases. It is also noteworthy that, although viscosity values increase with the biochar content, the optimization of the formulation composition has ensured that the viscosity remains well below the maximum allowable range for vat photopolymerisation techniques, between 800 and 1000 cP, as reported in literature. [7] This indicates that further modifications, including higher filler content, are still feasible.

Table 4. Zero-shear viscosity (η_0) of composites at 25°C (*evaluated at a shear rate of 10 1/s).

Sample Code	Viscosity [mPa*s]
A-IB	365*
A-IB+BC0.5	412*
A-IB+BC1	433*
A-IB+BC2	461*

5.3. 3D PRINTED COMPLEX STRUCTURES

In addition to the fundamental geometries necessary for characterization tests of printed samples, a variety of more intricate objects were successfully 3D printed, demonstrating excellent resolution and dimensional accuracy with both the A-IB resin and the formulations containing biochar. It is noteworthy that a consistent layer height of 0.100 mm was utilized for all printed geometries, which significantly contributed to the quality of the resulting moulds.

5.3.1. A-IB geometries

Starting with the formulation without filler, a helical complex of 450 layers was printed (Figure 43), reaching a height of 45 mm and successfully achieving a macroscopically identical geometry to that of the original CAD software model. This helical structure is characterized by intricate curvatures and smooth, continuous spirals, demonstrating the printer's capability to reproduce complex geometries with high fidelity. The design features both tight and wide turns, contributing to its overall structural complexity.

Subsequently, the same object was printed using all formulations to ensure replicability of the filled resin.

Figure 43. A-IB Helix 450 layers.

Additionally, a small vase, designated as Vase1, composed of 350 layers, and standing at 35 mm in height, was printed (Figure 44). This vase features a complex diagonal grid-like structure, characterized by a series of intersecting lines that create a dynamic pattern of

openings throughout its surface. Notably, Vase1 exhibits a variable diameter that changes with height. This object was then reprinted in different sizes using composite resins, as shown shortly.

Figure 44. A-IB Vase1 350 layers.

5.3.2. A-IB+BC0.5

With the resin enhanced by 0.5 phr of biochar, the same helical geometry of 450 layers (total height of 45 mm) achieved in the previous formulation was successfully replicated. Additionally, another vase geometry, referred to as Vase2, composed of 850 layers was also produced, resulting in a detail-rich shape with a height of 85 mm. Both geometries are illustrated in Figures 45 and 46, respectively.

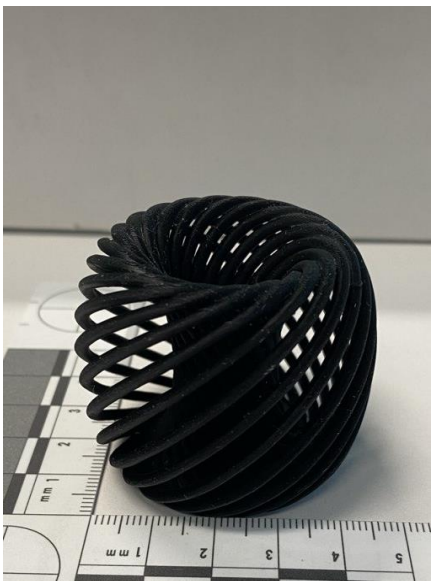

Figure 45. A-IB+BC0.5 - Helix 450 layers.

Figure 46. A-IB+BC0.5 - Vase2 850 layers.

Vase2 presents a different structural complexity. While it maintains the same external shape as Vase1, it features a distinctive texture. Instead of a diagonal grid pattern, it has a continuous mesh with holes of varying sizes, depending on the height position. This design resembles the pattern found in 3D-printed splints, which serve as alternatives to traditional casts.

5.3.3. A-IB+BC1

The formulation with 1 phr of biochar was used to print the helical structure with 450 layers (45 mm) and both Vase1 and Vase2, with different heights. The helical structure is depicted in Figure 47, while Figure 48 shows a top view of it. Vase 1, with 550 layers (55 mm), is shown in Figure 49, and Vase 2, with 650 layers (65 mm), is presented in Figure 50.

Figure 47. A-IB+BC1 - Helix 450 layers.

Figure 48. A-IB+BC1 - Details of the top of Helix.

Figure 49. A-IB+BC1- Vase1 550 layers.

Figure 50. A-IB+BC1 - Vase2 650 layers.

5.3.4. A-IB+BC2

Finally, using the last formulation with 2 phr of biochar, the helical complex of 450 layers was printed, as shown in Figure 51, along with Vase 2 consisting of 350 layers (Figure 52), achieving heights of 45 mm and 35 mm, respectively. In this case as well, excellent printing results were obtained, despite the higher concentration of incorporated filler.

Figure 51. A-IB+BC2 - Helix 450 layers.

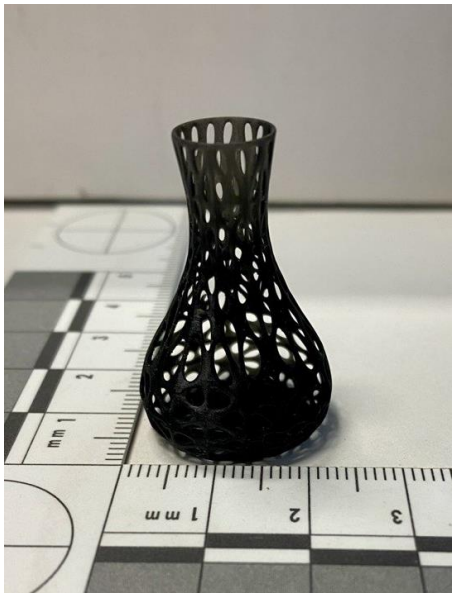

Figure 52. A-IB+BC2 – Vase2 350 layers.

Overall, all formulations demonstrated optimal print quality, confirming the effectiveness of the composite materials in achieving precise geometric fidelity. The helical complex consistently maintained its intricate geometry across the different formulations, illustrating the ability of biochar-infused resins to create complex structures while ensuring structural integrity. The parameters established for both formulation preparation and printing were optimal, resulting in good dimensional accuracy, even with the inclusion of the dark filler, which could have challenged the success of the printing process.

5.4. PHOTOCURED SPECIMENS' CHARACTERIZATION

5.4.1. Gel content percentage

Table 5 exhibits the gel content data comparison between A-IB, A-IB+BC0,5, A-IB+BC1, A-IB+BC2.

Table 5. Gel content data comparison.

Sample Code	Gel Content [%]
A-IB	99,7
A-IB+BC0.5	99,6
A-IB+BC1	99,6
A-IB+BC2	99,7

The data analysis does not reveal significant variations of the gel content values with the increase in biochar content, suggesting that the addition of the filler does not substantially affect the material's crosslinking degree.

It is worth noting to highlight that the gel content percentages are close to 100% for all the samples. Despite the black biochar potentially interfering with the photopolymerisation process by absorbing UV light, the chosen photoinitiator amount and printing parameters were effective in ensuring a high level of crosslinking.

5.4.2. Thermogravimetric analysis

The results of the thermogravimetric analysis on photocured specimens, varying the amount of incorporated biochar and without biochar, are presented in the following figures. Figure 53 illustrates the weight loss percentage and the degradation rate of the sample A-IB. In this thermogram, the initial weight loss of 5% occurs at a temperature of 279 °C, while the 50% and 90% weight losses occur at temperatures of 401°C and 558 °C, respectively. Regarding the maximum degradation rate, it occurs at a temperature of 317 °C.

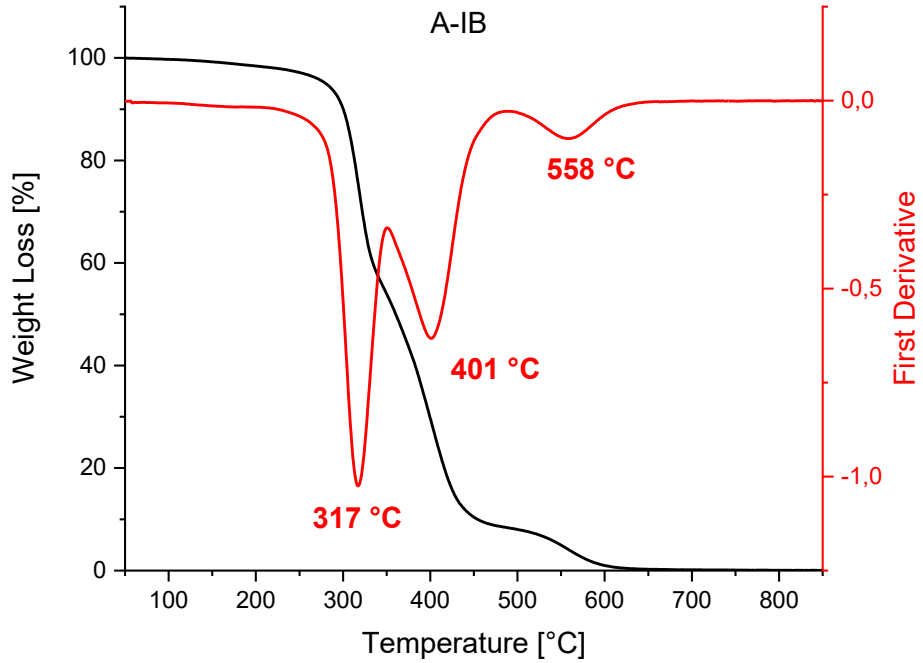

Figure 53. Weight Loss and Degradation rate of A-IB.

The TGA curves for the composites with 0.5, 1, and 2 phr of biochar are shown in Figures 54, 55, and 56, respectively, and the key data are extracted and summarized in Table 6.

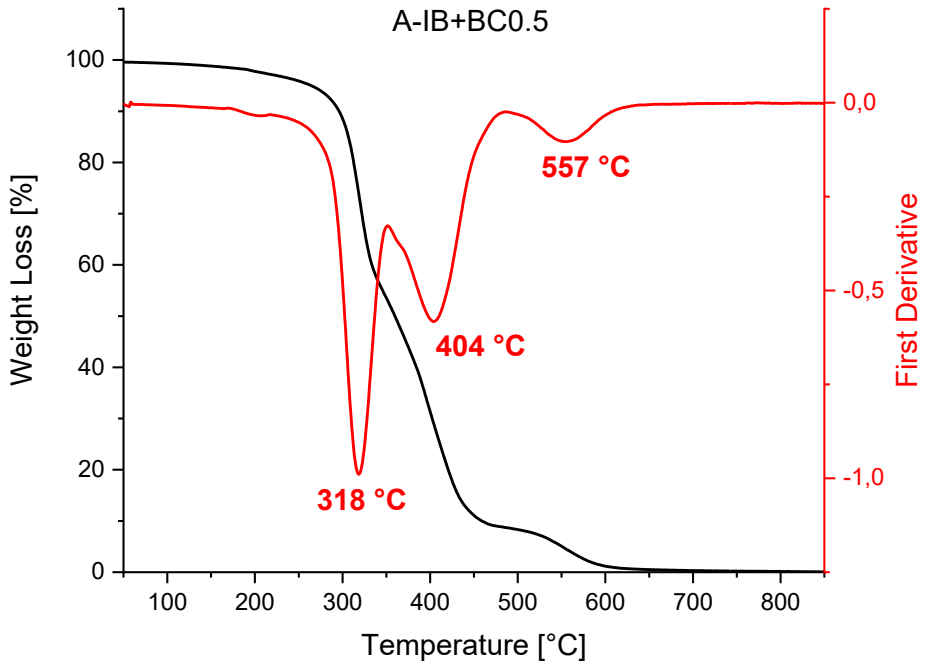

Figure 54. Weight Loss and Degradation rate of A-IB+BC0,5.

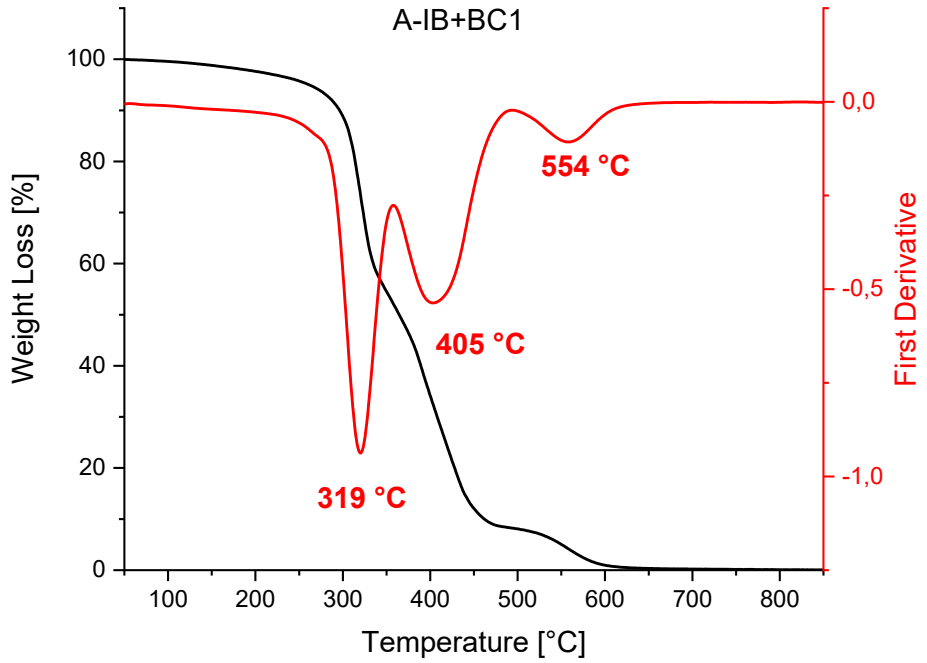

Figure 55. Weight Loss and Degradation rate of A-IB+BC1.

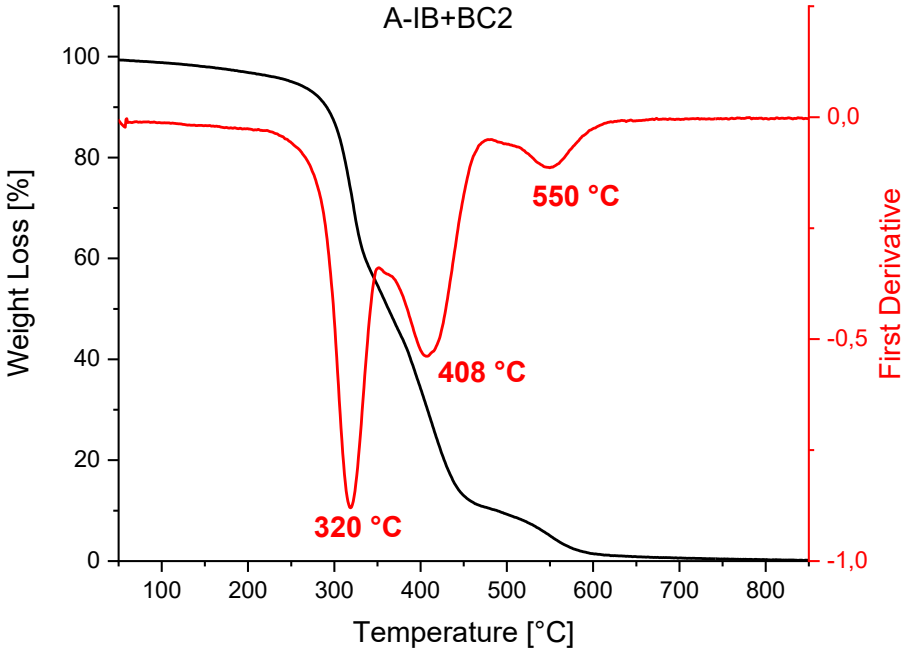

Figure 56. Weight Loss and Degradation rate of A-IB+BC2.

Table 6. Key data of TGA analyses.

Sample	T_{onset}*	$T_{degrmax}$	$T_{1°peak}$	$T_{2°peak}$	Ash
	[°C]	[°C]	[°C]	[°C]	[%]
A-IB	279	317	401	558	0
A-IB+BC0.5	264	318	404	557	0
A-IB+BC1	261	319	405	554	0
A-IB+BC2	251	320	408	550	0

*T_{onset} is the temperature at which a weight loss of 5% occurs.

From these data, it is noticeable that, compared to the A-IB specimens, those containing biochar show a slight decrease in T_{onset} as the biochar content increases, going from 279 °C in the A-IB resin to 264°C in A-IB+BC0.5. This value tends to decrease further to 261 °C and 251 °C for the specimens with 1 and 2 phr of biochar, respectively. This behaviour can be explained because the initial weight loss is usually due to the elimination of moisture or the release of volatile compounds. Since the filler is a derivative of cellulose pyrolysis, it introduces a certain internal porosity into the resin [61], which can retain more moisture, leading to greater weight loss at lower temperatures.

However, an improved situation is observed when looking at the temperature at which 50% weight loss occurs, which reaches 404 °C, 405 °C, and 408 °C for the 0.5, 1, and 2 phr biochar cases, respectively. This is also reflected in the temperature at which the maximum degradation peak occurs, which slightly increases by increasing the biochar content. This could indicate that, once moisture is removed from the samples, the higher biochar amount improves the thermal stability of the resin. Nevertheless, this improvement is not further evident in the final stage of the analysis, where the temperature at which 90% weight loss occurs decreases as the biochar content increases. A representative image comparing the specimens is shown in Figure 57.

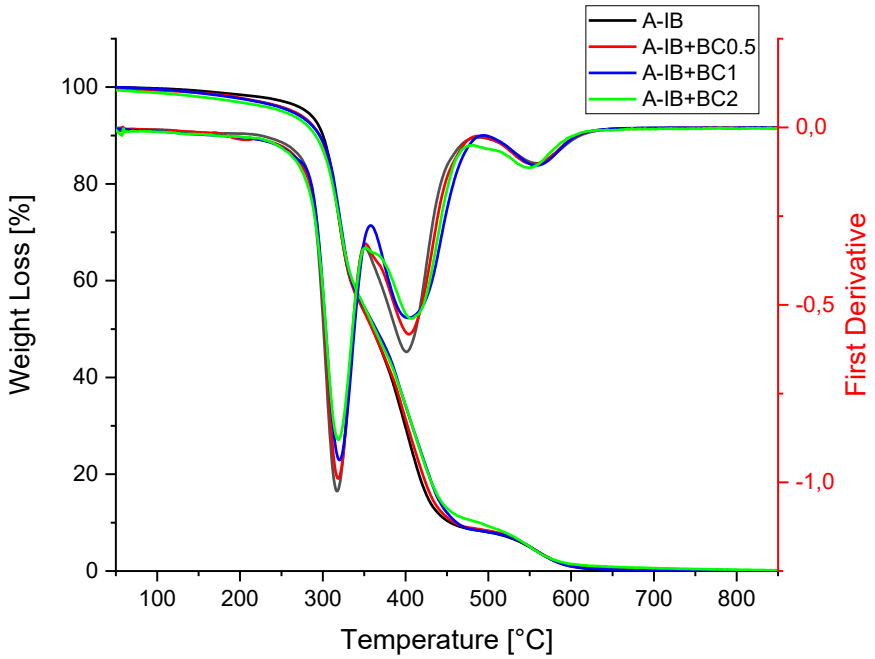

Figure 57. Comparison of TGA.

The ash content at the end of the analysis is zero for all specimens since both the biochar and the polymer formulations are organic materials without inorganic residues. This also confirms that no inorganic contamination occurred during the formulation preparation and printing process.

5.4.3. Differential scanning calorimetry

The DSC results for the different specimens are displayed in Figure 58. In this case, as the materials are thermosetting polymers, the only characteristic temperature that can be assessed is the glass transition temperature. Indeed, the curves do not exhibit any exothermic peaks associated with crystallization or endothermic peaks related to melting. Nevertheless, a slight variation in the slope of the curves, indicative of Tg, is observed in all the examined cases. Specifically, the temperatures at which the glass transition occurs have been extracted and summarized in Table 7.

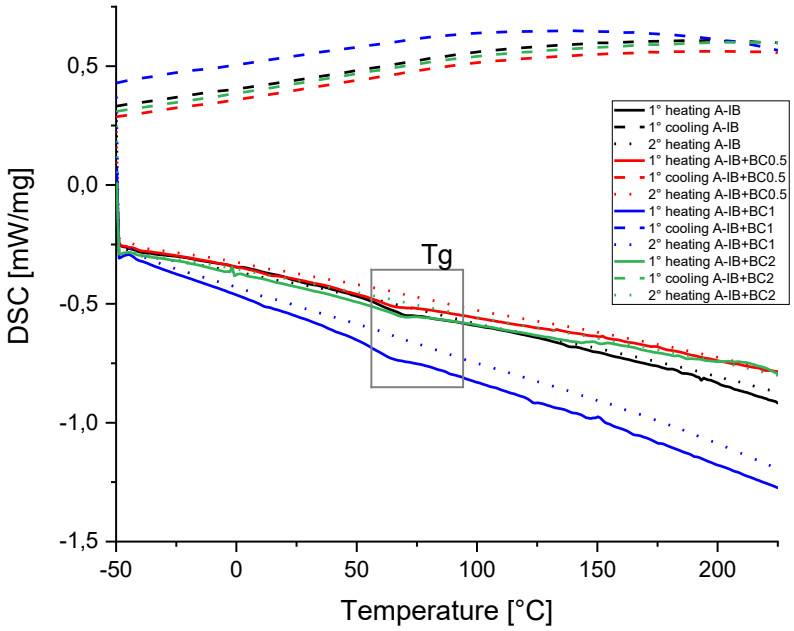

Figure 58. Comparison of DSC.

Table 7. Values of Tg for the different formulations.

Sample Code	Tg [°C]
A-IB	60
A-IB+BC0.5	70
A-IB+BC1	72
A-IB+BC2	73

It is observed that as the percentage of incorporated biochar increases, the Tg also slightly increases. In fact, starting from a value of 60 °C for the A-IB resin, it rises to 70 °C with the addition of only 0.5 phr of biochar, and further increases to 72 °C and 73 °C for the resins with 1 phr and 2 phr of filler, respectively.

5.4.4. Morphological analysis: FESEM

The results of the FESEM morphological analysis were obtained for specimens filled at 0.5 and 1 phr, as well as for unfilled specimens. Starting with the A-IB resin, observations were conducted at magnifications of 1000x (Figure 59) and 2000x, represented in Figure 60.

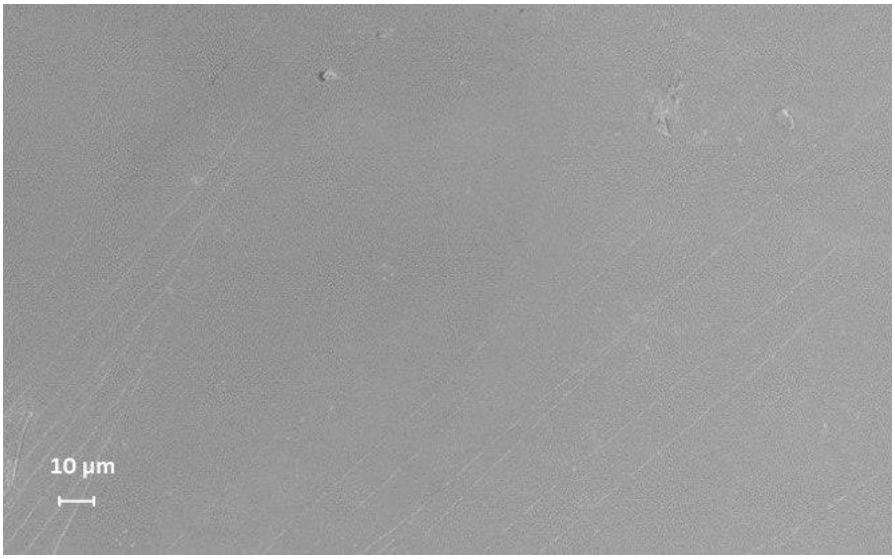

Figure 59. A-IB at 1000x.

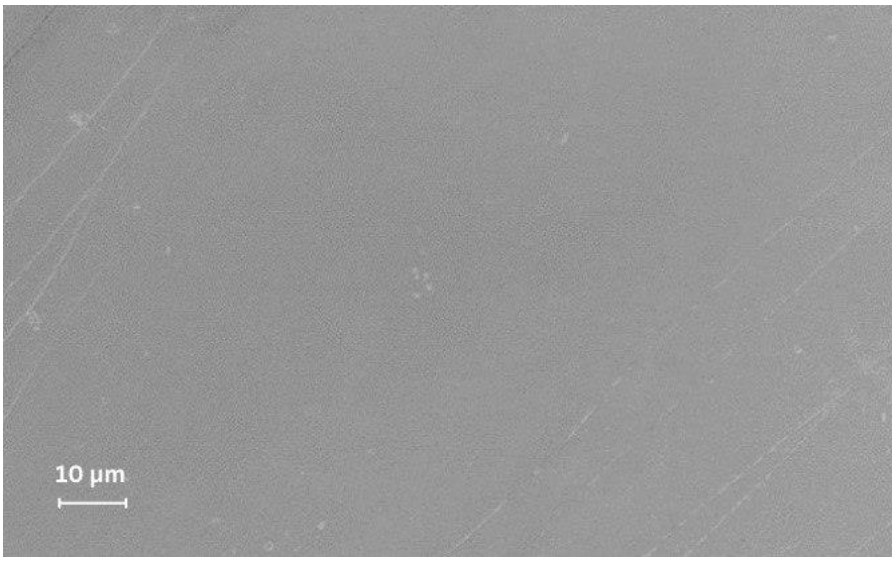

Figure 60. A-IB at 2000x.

In both cases, the fracture surfaces appear smooth and homogeneous since no filler has been incorporated. No signs of irregularities or defects are visible.

For the samples containing biochar, the fracture surface of the A-IB+BC1 sample, observed at a magnification of 5000x, shows that the filler is uniformly dispersed throughout the polymer matrix. Further examination at 100,000x reveals that the fracture surface exhibits a morphology with "defected spheres" embedded within the polymer matrix, which is no longer smooth and homogeneous as seen in the A-IB sample. Instead, the presence of biochar in the matrix is clearly visible, highlighting the spherical-like geometry of the filler. These findings are presented in Figure 61, with further magnification at 10,000x in Figure 62, and at 100,000x in Figure 63.

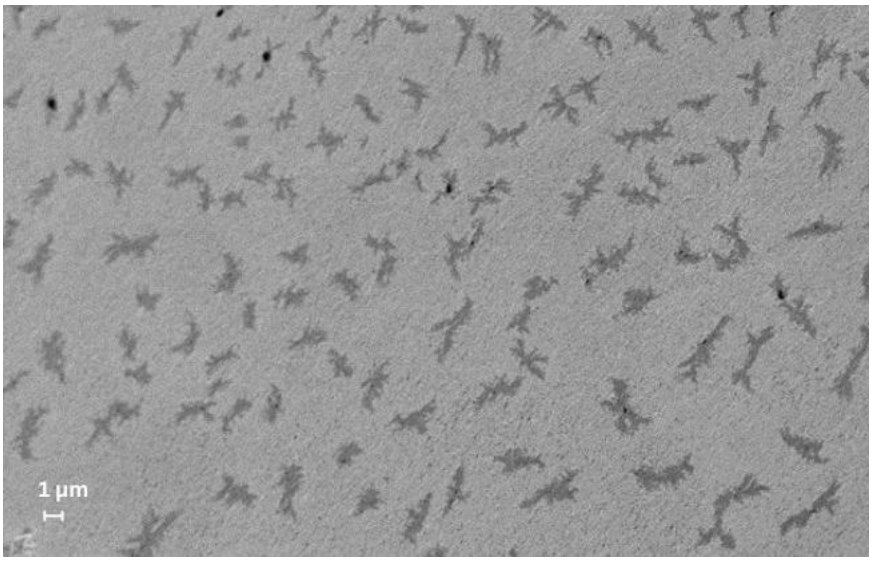

Figure 61. A-IB+BC1 at 5000x.

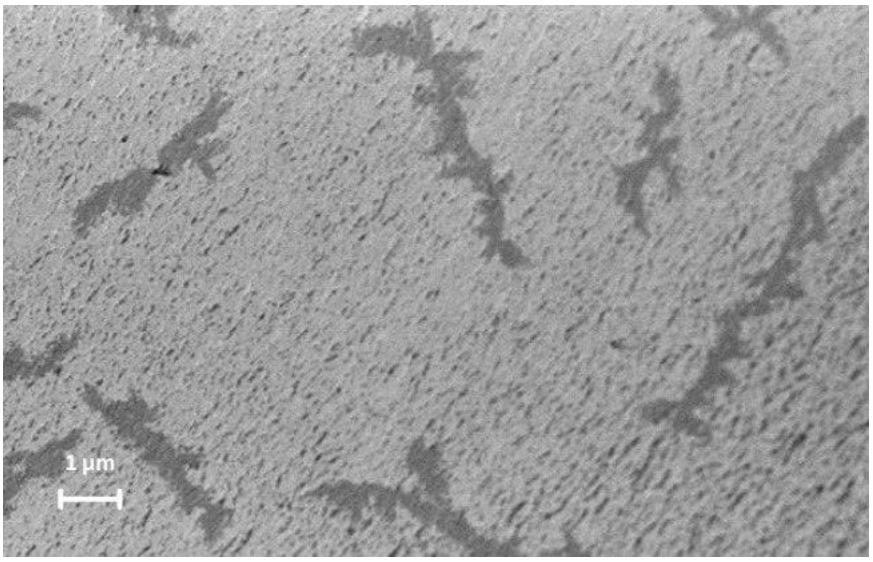

Figure 62. A-IB+BC1 at 10,000x.

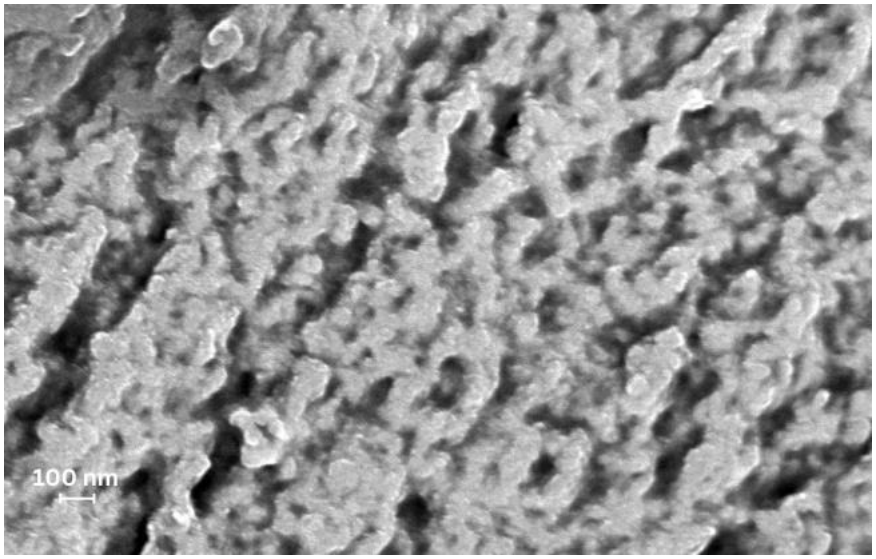

Figure 63. A-IB+BC1 at 100,000x.

Finally, in the case of biochar at 2 phr in the matrix, a similar morphology associated with the filler presence was observed at 100,000x magnification in Figure 66. However, when examining the fracture surface at 10,000x and 50,000x, shown in Figures 64 and 65 respectively, the same uniform distribution of carbon content is not evident. Instead, it appears to be clustered around the fracture surfaces of the specimens. This behaviour requires further analysis by assessing the mechanical properties of the composites.

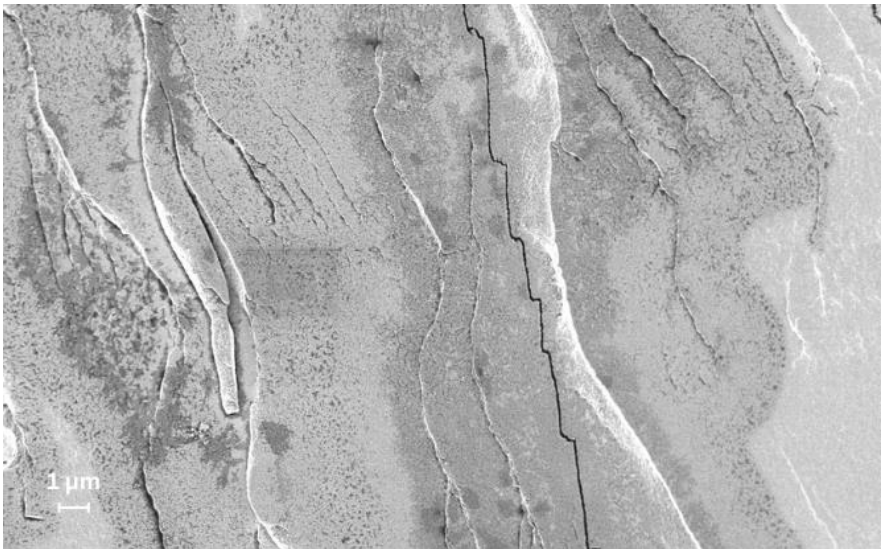

Figure 64. A-IB+BC2 at 10,000x.

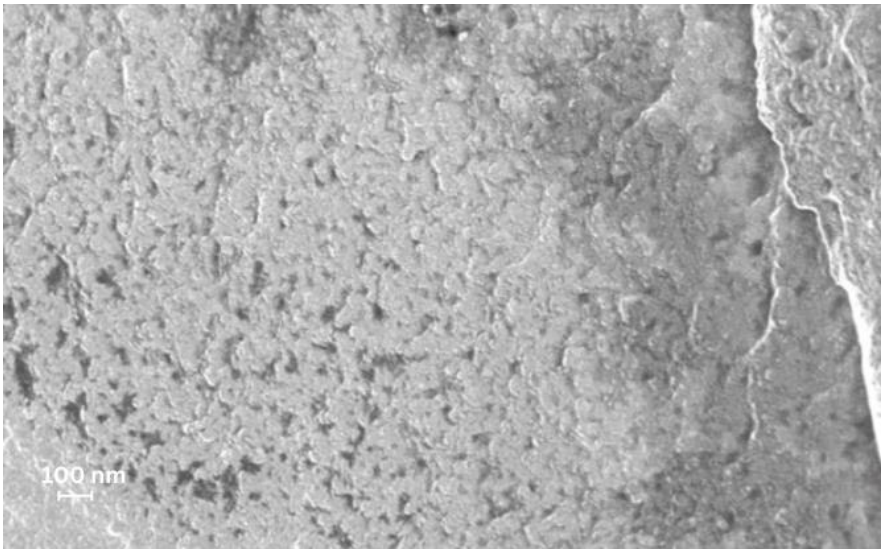

Figure 65. A-IB+BC2 at 50,000x.

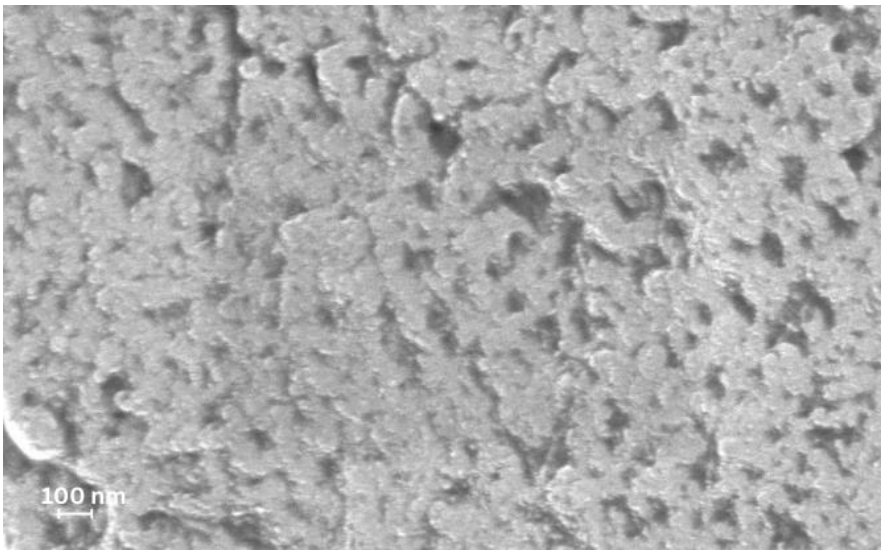

Figure 66. A-IB+BC2 at 100,000x.

5.4.5. Dynamic-mechanical thermal analysis

The results of the DMTA tests for each formulation are presented below. Specifically, Figure 67 displays the storage moduli, while Figures 68 and 69 illustrate the loss moduli and the extensional loss factors, respectively.

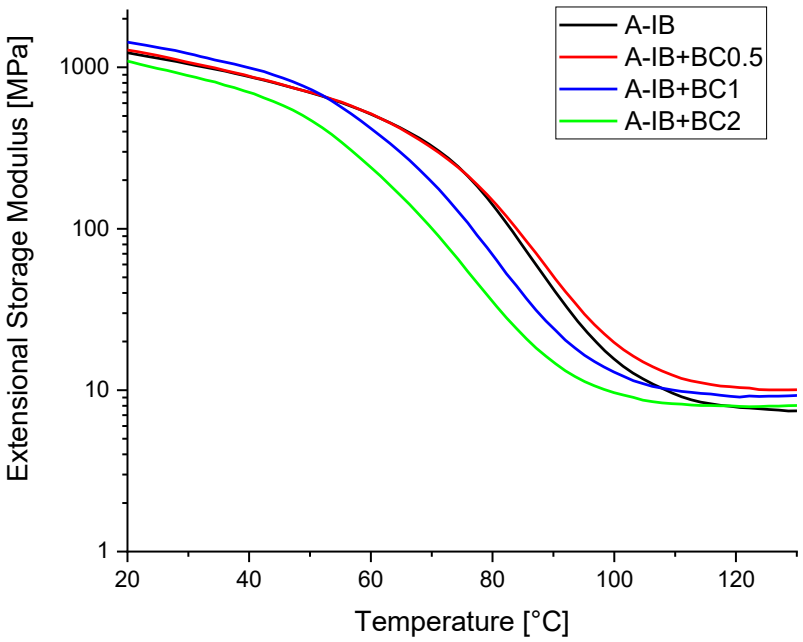

Figure 67. Storage moduli from DMTA.

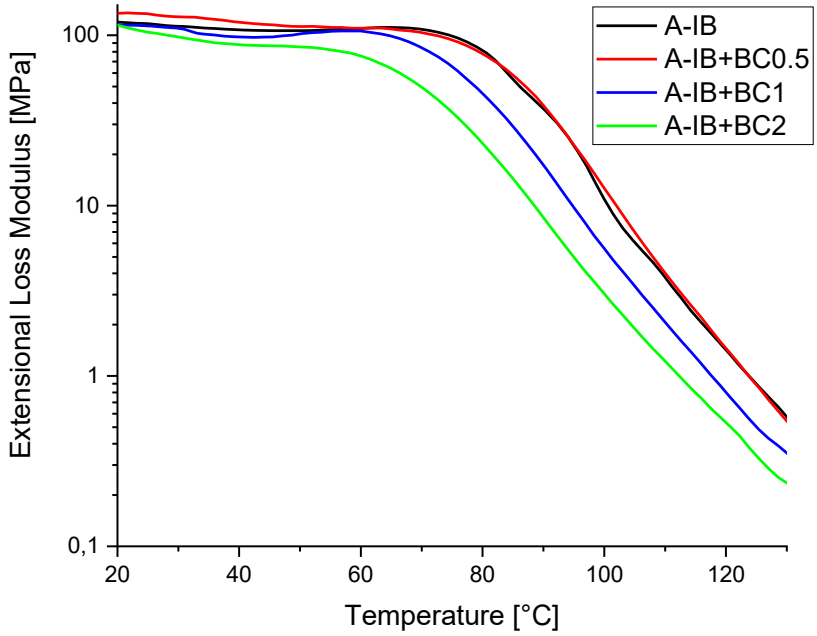

Figure 68. Loss moduli from DMTA.

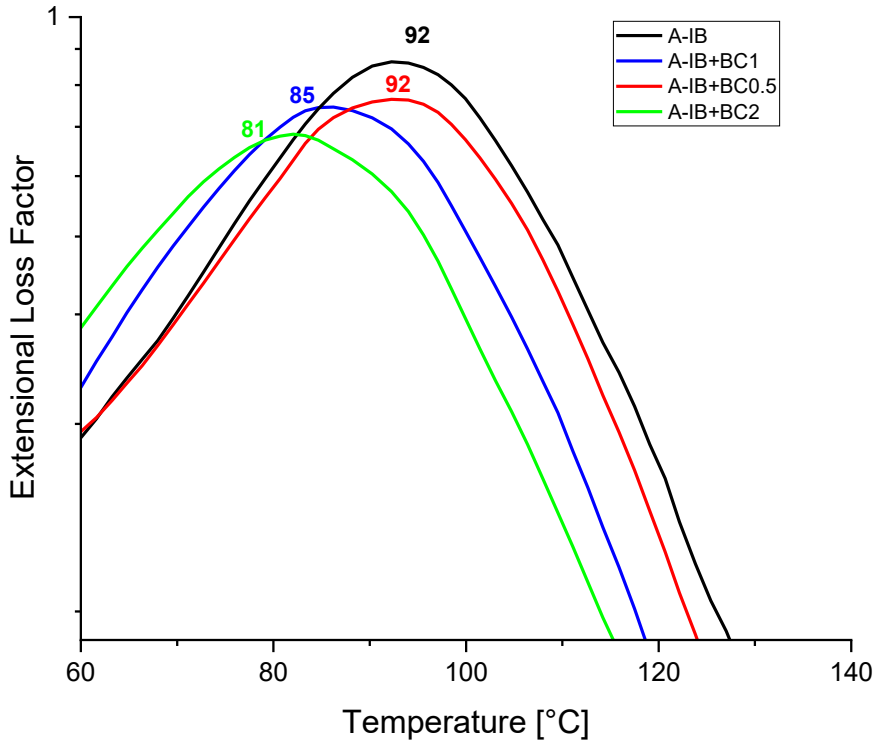

Figure 69. Extensional loss factors determined from DMTA.

A clear trend is observed: both the loss moduli and the storage moduli decrease with increasing temperature, indicating a reduction in both energy dissipation and elastic energy storage. This is characteristic of thermosetting polymers as they transition from a glassy state to a rubbery one. The temperature at which this transition occurs, marked by the maximum of the tan delta curve as a function of temperature, corresponds to the glass transition temperature (Tg), as previously shown in Figure 69 for each analysed specimen. The representative values from the analysis at 25 °C are summarized in Table 8.

Table 8. Representative data of DMTA. (*evaluated at 25°C)

Sample code	Storage Modulus*	Loss Modulus*	TanDelta
	[MPa]	[MPa]	[°C]
A-IB	1140	117	92
A-IB+BC0.5	1186	134	92
A-IB+BC1	1315	113	85
A-IB+BC2	984	104	81

The data shows that the storage modulus (E') is consistently higher than the loss modulus (E'') across all specimens, leading to a Tan delta value of less than one, which indicates predominantly elastic behaviour of the materials.

Interestingly, the peak values in the extensional loss factor curve slightly decreases by increasing the biochar content. This suggests that the sample analysed transitions more readily from the glassy state to the rubbery state as more filler is incorporated. This finding contrasts with the results obtained from DSC, where the Tg increases with biochar content. However, given the differing methodologies of these analyses, such discrepancies are not unexpected. Furthermore, the storage modulus increases as the biochar content rises from 0.5 to 1 phr, improving the mechanical properties of the polymer by allowing it to store more energy. However, with 2 phr of biochar, the storage modulus decreases compared to the 1 phr formulation, suggesting that while biochar initially improves mechanical performance, at higher concentrations (2 phr), the effect declines. One potential reason for this decline could be the clustering of biochar particles observed in the FESEM analysis at this concentration. These clusters may disrupt the effective dispersion of the filler within the polymeric matrix, resulting in a reduction in overall mechanical performance. This observation is further supported by the results of tensile testing.

5.4.6. Tensile tests

The results of the tensile tests in Table 9 highlight key trends in the mechanical properties of the various formulations, specifically focusing on Young's modulus, tensile strength, and elongation at break.

Table 9. Results of tensile tests.

Sample code	Young's modulus	Tensile strength	Elongation at break
	[MPa]	[MPa]	(%)
A-IB	634±42	29±1	7,5±1
A-IB+BC0.5	643±39	24±1	7,0±1
A-IB+BC1	679±40	22±1	7,0±1
A-IB+BC2	517±18	19±0	7,0±0

The introduction of biochar slightly increases the stiffness of the polymer. The Young's modulus rises from 634 MPa in the unfilled resin to 679 MPa in the formulation with 1 phr of biochar, indicating that small amounts of biochar enhance the rigidity of the material. However, when the content reaches 2 phr, the Young's modulus significantly decreases to 517 MPa. This suggests that an excessive amount of filler can lead to reduced stiffness, likely due to aggregation or inadequate dispersion, which aligns with the earlier DMA findings.

Tensile strength also decreases as the filler content increases. For the A-IB formulation, tensile strength measures 29 MPa, which drops to 24 MPa with 0.5 phr of biochar and continues to decrease to 19 MPa at 2 phr.

Similarly, the elongation at break also decreases by increasing the biochar content, from 8% in A-IB to 7% in A-IB+BC2. This suggests that the addition of filler reduces the polymer's ductility.

To summarize, the addition of biochar at 0.5 and 1 phr enhances the stiffness of the material, as indicated by the increased Young's modulus. However, this enhancement is accompanied by a decrease in both tensile strength and flexibility, as shown by the reduced elongation at break. As the biochar content increases to 2 phr, a notable decline in mechanical properties occurs, with both the modulus and tensile strength decreasing significantly. This suggests that there is a threshold for biochar incorporation, beyond which its presence adversely can impact the material performance.

CONCLUSION AND FUTURE PERSPECTIVES

In conclusion, the work focused on the exploration of new thermosetting polymer formulations based on plant materials, demonstrating their potential for use in 3D printing via LCD technology. This approach is more cost-effective than other vat polymerisation techniques while still achieving excellent results in terms of final resolution and printing speed.

The combination of AESO as the starting monomer, IBOMA as a reactive diluent, BAPO as a radical photoinitiator, and biochar as a bio-filler yielded composite formulations that exhibited excellent printing results in terms of both dimensional accuracy and surface finish, while also revealing interesting properties from morphological, rheological, mechanical, and thermal perspectives.

The results of the rheological tests indicated that the viscosity of the prepared formulations is compatible with the requirements of the printing process, ensuring optimal flow during the photopolymerisation process in LCD printer.

Printing tests, above all those involving complex geometries, demonstrated an excellent selection of parameters, despite the challenges posed by the absorption of UV light by biochar.

Investigations into the characteristics of the printed samples revealed that the incorporation of biochar at concentrations up to 1 phr led to good dispersion of the powder within the polymeric matrix, thereby enhancing the rigidity of the resulting composite materials. However, higher concentrations, such as 2 phr, exhibited negative effects, likely due to the formation of biochar clusters, as highlighted by FESEM, contributing to increase the material fragility, as also confirmed by tensile tests.

The thermal stability remains almost the same to underline that the addition of the filler at different concentrations does not have significantly effect on the final thermal behaviour. In conclusion, the results obtained highlight the significance of AESO-based polymers filled with biochar, printed via LCD technology, as a possible sustainable alternative to traditional synthetic thermosets. These materials not only offer a substantial reduction in environmental impact but also meet the performance demands required across various industrial applications. The AESO-based composite containing 1 phr of biochar stands out as a promising solution for producing eco-friendly products, thanks to

its enhanced mechanical properties and the excellent surface finish achieved during the printing process.

There is currently significant interest in the biomedical sector, where this material could be employed in the production of scaffolds or external orthopaedic braces. The basic resin, without fillers, has already shown optimal properties in cytotoxicity tests. However, it will be crucial to carry out further studies on the biochar-enriched version to validate its suitability for biomedical applications.

Furthermore, it may be advantageous to investigate the effect of biochar concentrations ranging from 1 to 2 phr to identify the optimal threshold that maximizes the improvement of mechanical, thermal, and morphological properties.

Simultaneously, considering the non-recyclability of traditional synthetic thermosetting resins, it becomes crucial to explore the degradability of these new materials to further enhance their sustainability profile.

This research represents an advance in the development of innovative polymer solutions capable of not only meeting performance requirements but also promoting more sustainable and environmentally friendly production technologies. By adopting these polymers in 3D printing, we can contribute to the creation of eco-friendly products, reducing the impact of non-renewable resources and fostering a more sustainable future that aligns with the needs of our generation and those to come.

BIBLIOGRAPHY

[1] C. Wang, H. Han, Y. Wu, and D. Astruc, "Nanocatalyzed upcycling of the plastic wastes for a circular economy," May 01, 2022, *Elsevier B.V.* doi: 10.1016/j.ccr.2022.214422.

[2] S. Nizamuddin and C. Chen, "Biobased, biodegradable and compostable plastics: chemical nature, biodegradation pathways and environmental strategy," Feb. 01, 2024, *Springer*. doi: 10.1007/s11356-023-31689-w.

[3] T. Narancic and K. E. O'Connor, "Plastic waste as a global challenge: Are biodegradable plastics the answer to the plastic waste problem?," Feb. 01, 2019, *Microbiology Society*. doi: 10.1099/mic.0.000749.

[4] "Plastics-the Facts 2022 OCTOBER 2022."

[5] "Sustainable development High-level political forum on sustainable development, convened under the auspices of the Economic and Social Council Progress towards the Sustainable Development Goals," 2023.

[6] "70/1. Transforming our world: the 2030 Agenda for Sustainable Development Transforming our world: the 2030 Agenda for Sustainable Development Preamble," 2015.

[7] M. Lebedevaite, V. Talacka, and J. Ostrauskaite, "High biorenewable content acrylate photocurable resins for DLP 3D printing," *J Appl Polym Sci*, vol. 138, no. 16, Apr. 2021, doi: 10.1002/app.50233.

[8] G. Odian, "PRINCIPLES OF POLYMERIZATION Fourth Edition."

[9] M. A. A. AlMaadeed, D. Ponnamma, and A. A. El-Samak, "Polymers to improve the world and lifestyle: physical, mechanical, and chemical needs," in *Polymer Science and Innovative Applications: Materials, Techniques, and Future Developments*, Elsevier, 2020, pp. 1–19. doi: 10.1016/B978-0-12-816808-0.00001-9.

[10] Michael. Niaounakis, *Biopolymers : products, processing, and applications*. William Andrew, imprint of Elsevier, 2015.

[11] E. Saldívar-Guerra and E. Vivaldo-Lima, "Introduction to Polymers and Polymer Types," Feb. 22, 2013, *John Wiley and Sons*. doi: 10.1002/9781118480793.ch1.

[12] J. P. Pascault and R. J. J. Williams, "Thermosetting Polymers," in *Handbook of Polymer Synthesis, Characterization, and Processing*, John Wiley and Sons, 2013, pp. 519–533. doi: 10.1002/9781118480793.ch28.

[13] S. Wang, S. Ma, Q. Li, W. Yuan, B. Wang, and J. Zhu, “Robust, Fire-Safe, Monomer-Recovery, Highly Malleable Thermosets from Renewable Bioresources,” *Macromolecules*, vol. 51, no. 20, pp. 8001–8012, Oct. 2018, doi: 10.1021/acs.macromol.8b01601.

[14] S. RameshKumar, P. Shaiju, K. E. O’Connor, and R. B. P, “Bio-based and biodegradable polymers - State-of-the-art, challenges and emerging trends,” Feb. 01, 2020, *Elsevier B.V.* doi: 10.1016/j.cogsc.2019.12.005.

[15] J. Liu, S. Wang, Y. Peng, J. Zhu, W. Zhao, and X. Liu, “Advances in sustainable thermosetting resins: From renewable feedstock to high performance and recyclability,” Feb. 01, 2021, *Elsevier Ltd*. doi: 10.1016/j.progpolymsci.2020.101353.

[16] S. Miao, P. Wang, Z. Su, and S. Zhang, “Vegetable-oil-based polymers as future polymeric biomaterials,” 2014, *Elsevier Ltd*. doi: 10.1016/j.actbio.2013.08.040.

[17] M. Bragaglia *et al.*, “Soybean Oil-Based 3D Printed Mesh Designed for Guided Bone Regeneration (GBR) in Oral Surgery,” *Macromol Biosci*, vol. 24, no. 5, May 2024, doi: 10.1002/mabi.202300458.

[18] G. Colucci, F. Sacchi, F. Bondioli, and M. Messori, “Fully Bio-Based Polymer Composites: Preparation, Characterization, and LCD 3D Printing,” *Polymers (Basel)*, vol. 16, no. 9, May 2024, doi: 10.3390/polym16091272.

[19] L. J. Tan, W. Zhu, and K. Zhou, “Recent Progress on Polymer Materials for Additive Manufacturing,” Oct. 01, 2020, *Wiley-VCH Verlag*. doi: 10.1002/adfm.202003062.

[20] R. Chaudhary, P. Fabbri, E. Leoni, F. Mazzanti, R. Akbari, and C. Antonini, “Additive manufacturing by digital light processing: a review,” Apr. 01, 2023, *Springer Science and Business Media Deutschland GmbH*. doi: 10.1007/s40964-022-00336-0.

[21] X. Zhang and F. Liou, “Introduction to additive manufacturing,” in *Additive Manufacturing*, Elsevier, 2021, pp. 1–31. doi: 10.1016/B978-0-12-818411-0.00009-4.

[22] J. Hu, D. Wang, and H. Peng, “Photoreaction Drives Efficient, Precise, and Sustainable Additive Manufacturing,” *Chem & Bio Engineering*, vol. 1, no. 5, pp. 414–426, Jun. 2024, doi: 10.1021/cbe.3c00126.

[23] *Additive manufacturing-General principles-Terminology*. 2017.

[24] J. Izdebska-Podsiadły, “Classification of 3D printing methods,” in *Polymers for 3D Printing: Methods, Properties, and Characteristics*, Elsevier, 2022, pp. 23–34. doi: 10.1016/B978-0-12-818311-3.00009-4.

[25] M. Spoerk, C. Holzer, and J. Gonzalez-Gutierrez, “Material extrusion-based additive manufacturing of polypropylene: A review on how to improve dimensional inaccuracy and warpage,” Mar. 20, 2020, *John Wiley and Sons Inc.* doi: 10.1002/app.48545.

[26] Y. Zhai, D. A. Lados, and J. L. Lagoy, “Additive Manufacturing: Making imagination the major Limitation,” *JOM*, vol. 66, no. 5, pp. 808–816, 2014, doi: 10.1007/s11837-014-0886-2.

[27] I. Echeta, X. Feng, B. Dutton, R. Leach, and S. Piano, “Review of defects in lattice structures manufactured by powder bed fusion,” *International Journal of Advanced Manufacturing Technology*, vol. 106, no. 5–6, pp. 2649–2668, Jan. 2020, doi: 10.1007/s00170-019-04753-4.

[28] O. Gülcan, K. Günaydın, and A. Tamer, “The state of the art of material jetting—a critical review,” Aug. 02, 2021, *MDPI AG*. doi: 10.3390/polym13162829.

[29] A. Davoudinejad, “Vat photopolymerization methods in additive manufacturing,” in *Additive Manufacturing*, Elsevier, 2021, pp. 159–181. doi: 10.1016/B978-0-12-818411-0.00007-0.

[30] C. Noè *et al.*, “DLP-printable fully biobased soybean oil composites,” *Polymer (Guildf)*, vol. 247, Apr. 2022, doi: 10.1016/j.polymer.2022.124779.

[31] M. Pagac *et al.*, “A review of vat photopolymerization technology: Materials, applications, challenges, and future trends of 3d printing,” Feb. 02, 2021, *MDPI AG*. doi: 10.3390/polym13040598.

[32] M. Bergoglio, Z. Najmi, A. Cochis, M. Miola, E. Vernè, and M. Sangermano, “UV-Cured Bio-Based Acrylated Soybean Oil Scaffold Reinforced with Bioactive Glasses,” *Polymers (Basel)*, vol. 15, no. 20, Oct. 2023, doi: 10.3390/polym15204089.

[33] X. Pan, M. A. Tasdelen, J. Laun, T. Junkers, Y. Yagci, and K. Matyjaszewski, “Photomediated controlled radical polymerization,” Nov. 01, 2016, *Elsevier Ltd*. doi: 10.1016/j.progpolymsci.2016.06.005.

[34] W. Piedra-Cascón, V. R. Krishnamurthy, W. Att, and M. Revilla-León, “3D printing parameters, supporting structures, slicing, and post-processing procedures of vat-polymerization additive manufacturing technologies: A narrative review,” Jun. 01, 2021, *Elsevier Ltd*. doi: 10.1016/j.jdent.2021.103630.

[35] N. Zhu *et al.*, “Preparation of complex SiOC ceramics by a novel photocurable precursor with liquid crystal display (LCD) 3D printing technology,” *J Eur Ceram Soc*, vol. 42, no. 7, pp. 3204–3212, Jul. 2022, doi: 10.1016/j.jeurceramsoc.2022.02.026.

[36] Z. Zhu, “Freeform Optics for Achieving Collimated and Uniform Light Distribution in LCD-Type UV-Curable 3D Printing,” *IEEE Photonics J*, vol. 15, no. 4, Aug. 2023, doi: 10.1109/JPHOT.2023.3294478.

[37] Y. Li, X. Ren, L. Zhu, C. Li, and T. Lin, “Synthesis and characterization of polyurethane acrylate with bio-oil modification for photo-curing 3D printed flexible structures,” *Polymer (Guildf)*, vol. 306, Jun. 2024, doi: 10.1016/j.polymer.2024.127225.

[38] M. IN HET PANHUIS *et al.*, "A COMPOSITE FROM SOY OIL AND CARBON NANOTUBES," *Int J Nanosci*, vol. 02, no. 03, pp. 185–194, Jun. 2003, doi: 10.1142/s0219581x0300119x.

[39] "412333-BULK".

[40] "392111-BULK_____ALDRICH__IBOMA".

[41] M. Alsaadi *et al.*, "Liquid-Based 4D Printing of Shape Memory Nanocomposites: A Review," Feb. 01, 2023, *MDPI*. doi: 10.3390/jmmp7010035.

[42] "511447-BULK_____ALDRICH__BAPO".

[43] M. Lebedevaite and J. Ostrauskaite, "Influence of photoinitiator and temperature on photocross-linking kinetics of acrylated epoxidized soybean oil and properties of the resulting polymers," *Ind Crops Prod*, vol. 161, Mar. 2021, doi: 10.1016/j.indcrop.2020.113210.

[44] Q. Zhang *et al.*, "Biochar filled high-density polyethylene composites with excellent properties: Towards maximizing the utilization of agricultural wastes," *Ind Crops Prod*, vol. 146, Apr. 2020, doi: 10.1016/j.indcrop.2020.112185.

[45] Z. Mohammed, S. Jeelani, and V. Rangari, "Effective reinforcement of engineered sustainable biochar carbon for 3D printed polypropylene biocomposites," *Composites Part C: Open Access*, vol. 7, Mar. 2022, doi: 10.1016/j.jcomc.2021.100221.

[46] A. Alhelal, Z. Mohammed, S. Jeelani, and V. K. Rangari, "3D printing of spent coffee ground derived biochar reinforced epoxy composites," *J Compos Mater*, vol. 55, no. 25, pp. 3651–3660, Oct. 2021, doi: 10.1177/00219983211002237.

[47] M. Giorcelli, P. Savi, A. Khan, and A. Tagliaferro, "Analysis of biochar with different pyrolysis," *INTERNATIONAL JOURNAL OF QUALITY AND RELIABILITY MANAGEMENT*, doi: 10.1108/IJQRM.

[48] S. Greenough, M. J. Dumont, and S. Prasher, "The physicochemical properties of biochar and its applicability as a filler in rubber composites: A review," Dec. 01, 2021, *Elsevier Ltd*. doi: 10.1016/j.mtcomm.2021.102912.

[49] M. Bartoli *et al.*, "Shape tunability of carbonized cellulose nanocrystals," *SN Appl Sci*, vol. 1, no. 12, Dec. 2019, doi: 10.1007/s42452-019-1727-2.

[50] M. Bartoli, R. Arrigo, G. Malucelli, A. Tagliaferro, and D. Duraccio, "Recent Advances in Biochar Polymer Composites," Jun. 01, 2022, *MDPI*. doi: 10.3390/polym14122506.

[51] "Anycubic_Wash_Cure_Machine_Man (1)".

[52] "Standard Test Methods for Determination of Gel Content and Swell Ratio of Crosslinked Ethylene Plastics 1", doi: 10.1520/D2765-16.

[53] T. . Hatakeyama and F. X. . Quinn, *Thermal analysis : fundamentals and applications to polymer science*. John Wiley & Sons, 2000.

[54] M. Isola, G. Colucci, A. Diana, A. Sin, A. Tonani, and V. Maurino, "Thermal properties and decomposition products of modified cotton fibers by TGA, DSC, and Py–GC/MS," *Polym Degrad Stab*, vol. 228, Oct. 2024, doi: 10.1016/j.polymdegradstab.2024.110937.

[55] J. D. Menczel *et al.*, "Fundamentals of DSC," in *Handbook of Differential Scanning Calorimetry: Techniques, Instrumentation, Inorganic, Organic and Pharmaceutical Substances*, Elsevier, 2023, pp. 1–189. doi: 10.1016/B978-0-12-811347-9.00005-9.

[56] S. Jodeh, "Carrier films behavior during thermoforming process studied using dynamic mechanical thermal analysis (DMTA)," *Journal of Polymer Research*, vol. 18, no. 5, pp. 939–944, Sep. 2011, doi: 10.1007/s10965-010-9491-4.

[57] G. Bussu and A. Lazzeri, "On the use of dynamic mechanical thermal analysis (DMTA) for measuring glass transition temperature of polymer matrix fibre reinforced composites," *J Mater Sci*, vol. 41, no. 18, pp. 6072–6076, Aug. 2006, doi: 10.1007/s10853-006-0694-3.

[58] "Designation: D7028 − 07 Standard Test Method for Glass Transition Temperature (DMA Tg) of Polymer Matrix Composites by Dynamic Mechanical Analysis (DMA) 1", doi: 10.1520/D7028-07R24.

[59] "ISO 527-2".

[60] D. Brabazon and A. Raffer, "Emerging Nanotechnologies for Manufacturing", Chapter 3, pp. 59-91, Knover, 2010.

[61] K. Weber and P. Quicker, "Properties of biochar," Apr. 01, 2018, *Elsevier Ltd*. doi: 10.1016/j.fuel.2017.12.054.